THE JOURNAL OF PHYSICAL CHEMISTRY B

pubs.acs.org/JPCB Article

Characterizing the Brownian Diffusion of Nanocolloids and Molecular Solutions: Diffusion-Ordered NMR Spectroscopy vs Dynamic Light Scattering

Chengqi Zhang, Zhicheng Jin, Birong Zeng, Wentao Wang, Goutam Palui, and Hedi Mattoussi*

Cite This: J. Phys. Chem. B 2020, 124, 4631−4650 Read Online

ABSTRACT: Hydrodynamic size is a characteristic dimension that reflects the Brownian diffusion of objects, such as proteins, macromolecules, and various colloids when dissolved/dispersed in fluid phases. This property is crucial when investigating the utility of colloidal nanocrystals and polymeric materials in biology. Dynamic light scattering (DLS) has been widely used to measure the diffusion coefficient and hydrodynamic size of such systems. Comparatively, diffusion-ordered NMR spectroscopy (DOSY-NMR) is a relatively new analytical method that has provided researchers with an alternative experimental approach to access such information. Here, we apply DLS and DOSY-NMR simultaneously to characterize the diffusion coefficient and hydrodynamic size of several sets of nanocolloids, including dispersions of gold nanoparticles and luminescent quantum dots that are surface-capped with either hydrophobic or hydrophilic coatings, as well as a monomer and a low-molecular-weight polymer. We compare, side by side, the findings acquired from each measurement, which has allowed us to identify the benefits and constraints of each technique. Our results show that the two approaches provide comparable data when larger size nanocolloids are probed. However, we find that DOSY is substantially more effective in characterizing nanocolloids that are fluorescent and/or have very small dimensions, as well as molecular-scale organic ligands, where DLS reaches its limit. Additionally, we find that, compared to DLS, DOSY tends to require higher solute concentrations and longer collection time to generate data with high signal-to-noise ratios.

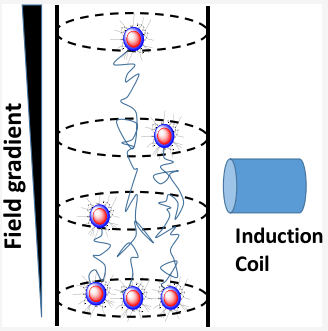

INTRODUCTION

Colloidal nanocrystals grown using bottom-up, solution phase methods, such as gold nanoparticles (AuNPs) and luminescent semiconductor quantum dots (QDs), have been integrated into a variety of applications ranging from electronic devices to sensor and imaging probe designs in biology.[1−10] These applications exploit some of the unique size- and shape-dependent optical and spectroscopic properties exhibited by these materials.[2,3,7,8,11−20] The surfaces of such nanocolloids are engineered to present coatings made of molecular-scale or polymer ligands (hydrophobic, amphiphilic, or hydrophilic), which promote the dispersion of these materials in solutions. Such coatings promote long-term colloidal stability and control the nanoparticle (NP) interactions with biological media. They also facilitate conjugation to various targeted molecules, yielding hybrid, biologically active nanoparticle constructs. One of the key parameters often needed to understand and control the behavior of these colloids, either in solution or integrated within biological media (e.g., in buffer media, serum, and cell media), is a reliable determination of their hydrodynamic size. This is a characteristic dimension that reflects the Brownian motion of these nanomaterials in fluid phases. Such property often describes the contribution of the organic coating to the overall mobility of the nanocrystals and the interactions of the colloids with the surrounding medium. In biological media, it also accounts for the effects of nonspecific adsorption of biomolecules on the nanocrystal surfaces.[21,22] Therefore, developing an accurate and reliable analytical characterization of the hydrodynamic size of such small colloids when dispersed in solution phases is crucially important, both for understanding the behavior of these materials in various systems, biological and nonbiological alike, and for improving their stability and reactivity.[23−26]

Conventional high-resolution analytical methods, such as transmission electron microscopy (TEM) and static small-angle X-ray scattering (SAXS), are effective techniques to characterize the dimensions of the inorganic component of these complex and very small colloids; they tend to overlook/ignore the contribution of the organic ligand shell.[27,28] Comparatively, dynamic light scattering (DLS), also known as photon correlation spectroscopy, or quasi-elastic light scattering, has been widely used to extract information about the Brownian diffusion coefficient (and hydrodynamic size) along with the

Received: March 11, 2020
Revised: April 27, 2020
Published: May 1, 2020

https://dx.doi.org/10.1021/acs.jpcb.0c02177
J. Phys. Chem. B 2020, 124, 4631−4650

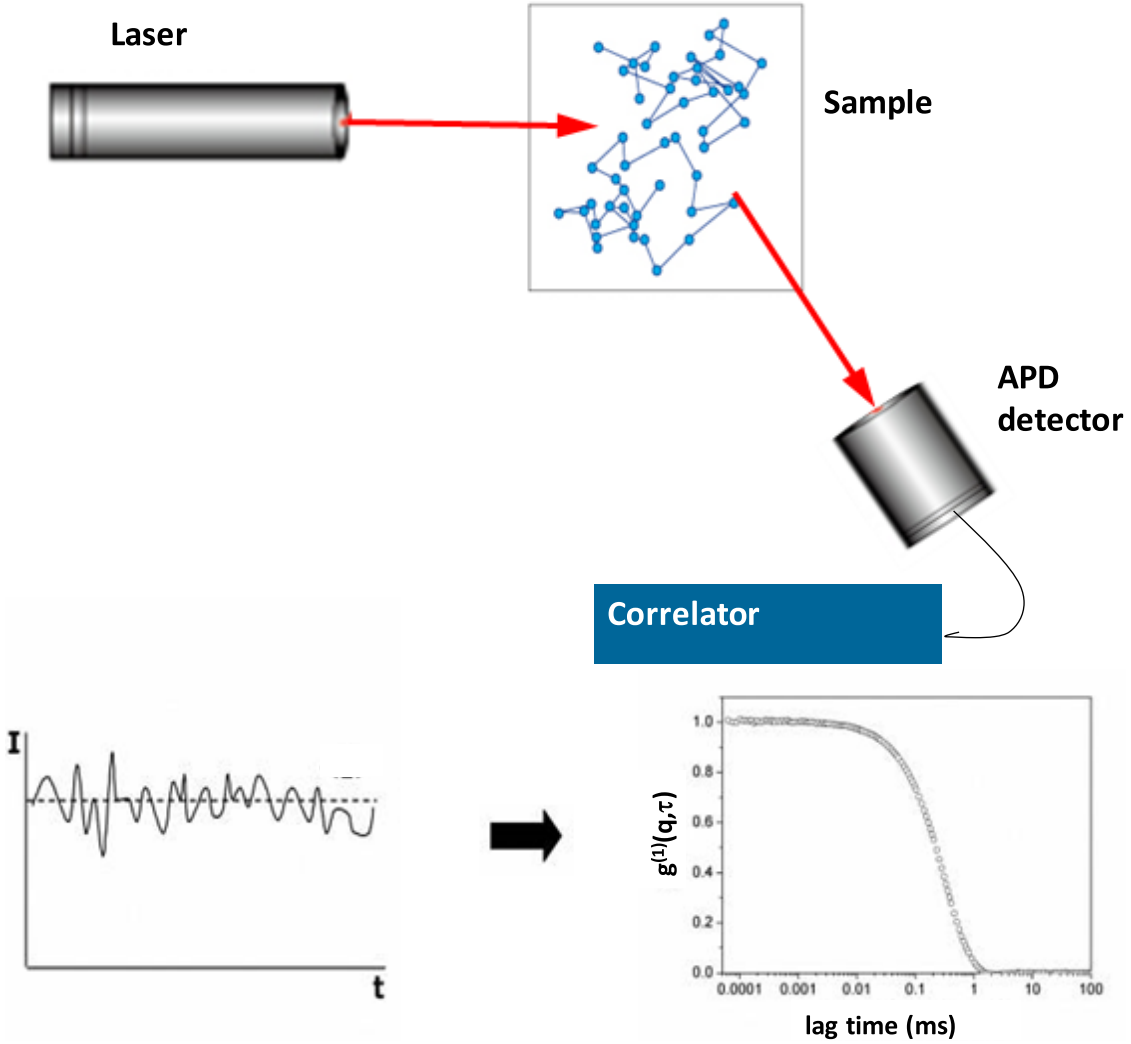

Figure 1. Schematic representation of the main steps involved in a dynamic light scattering measurement. Following irradiation of the sample with a laser source, the fluctuating scattered signal collected at a given angle with respect to the incident beam (bottom left) is used to construct the time-dependent normalized autocorrelation function, $g^{(1)}(\theta,\tau)$, shown in the bottom right.

interaction parameters for solutions of proteins, macromolecules, liposomes, and colloids with sizes of ∼10−1000 nm.[29,30] However, the technique encounters serious limitations when probing very small solute objects (e.g., nanocrystals with diameters <2 nm or low-molecular-weight polymers), due to a drop in the measured scattered signals.[29−31] Moreover, when this technique is applied to a fluorescent material (e.g., orange- and red-emitting QDs), the sample emission interferes with the scattered laser signal, which complicates data analysis and yields unreliable information. In this scenario, fluorescence correlation spectroscopy (FCS) can be used to circumvent this issue. However, a careful understanding of single molecule emission is required for data processing and analyses.[22,32−35]

The development of diffusion-ordered spectroscopy (DOSY), a two-dimensional (2D) nuclear magnetic resonance (NMR) technique (also referred to as spin echo), has opened new opportunities to characterize the diffusion properties of colloids and other solute materials over a broad size range. Because the technique does not exploit a size-dependent signal, but instead it correlates changes in the NMR signals of specific atoms/groups within larger structures (e.g., polymers and nanoparticles) to their Brownian motion, DOSY provides an effective means to measure the diffusion coefficient of various solute materials. Additionally, this method allows access to a wide size range and can be applied to fluorescent objects, such as luminescent quantum dots. Hens, Martins, and co-workers have pioneered the use of NMR techniques to probe the dynamic of ligand interactions with nanocolloids, identify binding site heterogeneity, and track ligand competition for surface coordination in QD dispersions.[36−38] They also used DOSY to probe the diffusion of ligands in nanoparticle suspensions, characterize bound oleate ligands on QDs, and measure the hydrodynamic size of these nanomaterials.[39−41] Similarly, our group used DOSY to monitor the purification of QDs and identify the nature of the bound ligands.[42−44] In particular, we showed that DOSY can distinguish between bound and free ligands in the medium, based on differences in the translational diffusion coefficients, associated with specific protons in the coating ligands.

In this study, we carry out a side-by-side comparison between similarities and differences of DLS and DOSY-NMR when applied to characterize various materials, including metallic AuNPs, luminescent CdSe core-only and CdSe−ZnS core−shell QDs, low-molecular-weight polymers, and molecular-scale ligands. We provide the mathematical rationales and combine these with data from several representative samples to draw a

https://dx.doi.org/10.1021/acs.jpcb.0c02177
J. Phys. Chem. B 2020, 124, 4631−4650

complete picture of the "pros and cons" of each technique. In particular, we show that, while both techniques provide reliable data when probing dispersions of larger size solutes, DLS tends to fail when the probed dispersions/solutions contain rather small objects (e.g., core-only QDs and low-molecular-weight polymers). However, DOSY-NMR can still yield reliable information for smaller nanocrystals and molecular-scale solute objects.

EXPERIMENTAL SECTION

Background. *Dynamic Light Scattering.* It has been established that when a sample, with inherent inhomogeneities, is subjected to electromagnetic irradiation, an elastically scattered signal can be measured; the signal originates from the scattering centers in the medium, as originally proposed by Rayleigh.[29,45,46] The Rayleigh model also predicts that the amplitude of the scattered intensity varies as the sixth power of the solute object size (e.g., the radius of a sphere).[29] Furthermore, if a fluid sample such as a solution of proteins or a dispersion of nanoparticles is used, fluctuations in the concentration of scattering centers are time-dependent, due to the Brownian motion, which yields a time-dependent Rayleigh signal. In addition to size, light scattering inherently depends on the polarizability contrast between the solute objects and the surrounding solvent molecules, which can be simply accounted for through the refractive index increment of the solution/dispersion with respect to solvent alone, normalized to concentration, dn/dc. Thus, to be effective, DLS measurements require a nonzero value for dn/dc.[29,47]

Dynamic light scattering exploits the time-dependent fluctuations in the scattered intensity to extract a measure of the solute diffusion coefficient and information about the polydispersity index (PDI). In a routine DLS experiment, the autocorrelation function of the scattered intensity, at an angle θ with respect to the incident beam (see schematics in Figure 1), $I_s(q,\tau)$, is built from the scattered signal using[46]

$$g^{(2)}(q,\tau) = \frac{\langle I_s(q,t) I_s(q,t+\tau)\rangle_t}{\langle I_s(q,t)\rangle_t^2} \tag{1}$$

where $\langle\cdots\rangle_t$ denotes the average over time and q is the scattering wavevector expressed in terms of θ, the incident laser wavelength, λ, and the medium refractive index, n, with $q = \frac{4\pi n}{\lambda}\sin\left(\frac{\theta}{2}\right)$. From this, one can extract a measure for the electric field autocorrelation function

$$g^{(1)}(q,\tau) = \frac{\langle E_s(q,t) E_s(q,t+\tau)\rangle_t}{\langle E(q,t)\rangle_t^2}$$

using the relation

$$g^{(1)}(q,\tau) = a|g^{(2)}(q,\tau) - 1|^{1/2} \tag{2}$$

where the constant a is proportional to the amplitude of the scattered signal.

When inhomogeneities in the size and/or molecular weight (MW) of the solute objects are present (which is always the case), the autocorrelation function exhibits a departure from the ideal single-exponential decay expected for a monodisperse sample. Size distribution can be described using, for example, Gaussian or log-normal distribution functions.[30] To account for the effects of size inhomogeneities, the autocorrelation function is then best-fit to a cumulant series[30,48]

$$g^{(1)}(q,\tau) = a\, e^{(-\Gamma\tau + (\mu_2/2)\tau^2 + \cdots)} \tag{3}$$

where the first cumulant is the average decay rate, Γ, and the second cumulant μ_2 provides a measure of the polydispersity index defined as

$$\mathrm{PDI} \equiv \left(\frac{\text{size distr. width}}{\text{mean size}}\right)^2 = \frac{\mu_2}{\Gamma^2} \tag{4}$$

The decay rate Γ depends on the diffusion coefficient, D, and the wavevector, q, via the relation: $\Gamma = Dq^2$. The above procedure can be applied at several angles, yielding multiple measurements of D for a given sample, which increases the accuracy of the reported value.[29,31,47]

A further refined analysis of the scattered data that accounts for the size dispersity of the sample uses the Laplace transform of the autocorrelation function, which can be written as

$$G(\Gamma) = \int g^{(1)}(q,\tau)\, e^{\Gamma\tau}\, d\tau \tag{5}$$

Representation of the Laplace transform function, $G(\Gamma)$, for a homogeneous dispersion of nanoparticles (or a solution of macromolecules) would provide a discrete peak centered at the decay rate (or diffusion coefficient) of the solute species. This approach is routinely used to plot the scattering data as a histogram of the intensity vs hydrodynamic radius, R_H, using the Stokes–Einstein relation[29]

$$D = \frac{k_B T}{f_T} = \frac{k_B T}{6\pi\eta R_H} \text{ and } R_H = \frac{k_B T}{6\pi\eta D} \tag{6}$$

where k_B, f_T, and η are the Boltzmann constant, the friction coefficient, and the solvent viscosity, respectively. Here, the width of the peak reflects the effects of the PDI value on the measured scattering data.

The DLS data are often acquired using a small but finite concentration (i.e., dilute regime). The effects of interparticle interactions in sterically stabilized samples are small, yet not negligible. When these interactions are accounted for using, for instance, the second virial coefficient, one can express the diffusion coefficient (or R_H), often referred to as an apparent (concentration-dependent) diffusion coefficient, $D_{app}(c)$, as

$$D_{app} = D_0(1 + Kc) \text{ or } R_H = R_H^0(1 - Kc) \tag{7}$$

where c, D_0, and R_H^0, respectively, are the concentration, diffusion coefficient, and hydrodynamic radius of isolated objects (measured at the limit of $c = 0$), and K is the interaction parameter that depends on the second virial coefficient.[29]

The DLS measurements presented in this study were carried out using an ALV/CGS-3 compact goniometer system from ALV-GmbH (Langen, Germany). The scattering setup is equipped with a He–Ne laser source (λ = 633 nm), an avalanche photodiode (APD) for signal detection, and a variable delay time (multi-τ) ALV-7004 photon correlator used to build the autocorrelation function, $g^{(1)}(q,\tau)$. The scattered signal, consisting of the average of three acquisition periods of 10 s each, was collected at several angles ranging between 25 and 140°. The autocorrelation function, generated from the scattered intensity profiles, was fitted to a cumulant series using ALV software. For every sample, we verified that the measured hydrodynamic size, extracted from the Laplace transform, $G(\Gamma)$, is independent of the scattering angle, as anticipated.[31] The data on the hydrodynamic size reported throughout the report were acquired at a 90° scattering angle,

https://dx.doi.org/10.1021/acs.jpcb.0c02177
J. Phys. Chem. B 2020, 124, 4631–4650

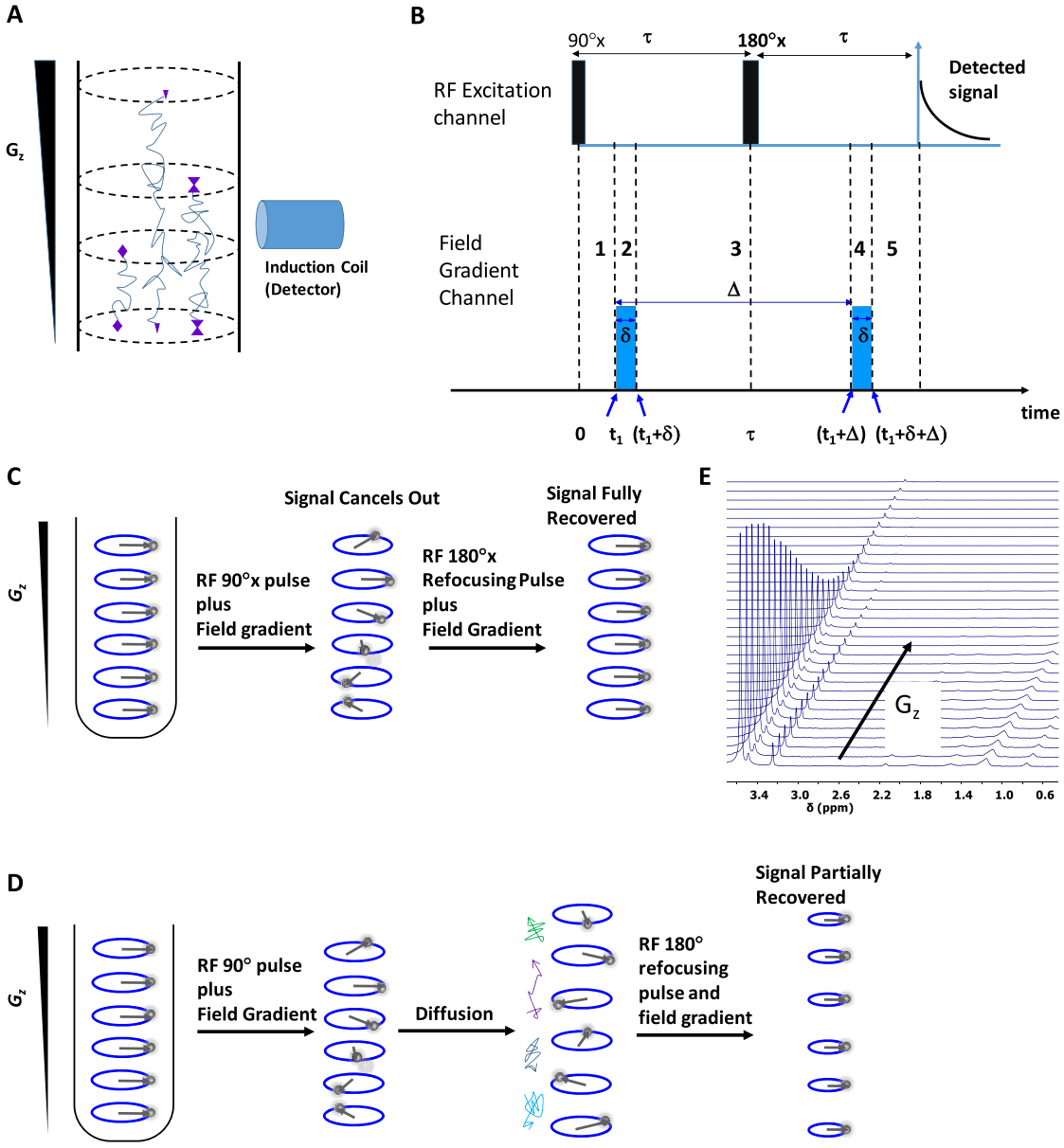

Figure 2. Schematics of the principles governing diffusion-ordered NMR spectroscopy. (A) Schematic of the DOSY-NMR experimental setup and the effects of spin diffusion. (B) RF pulse and field gradient sequences applied to the sample. (C) Sequence produces no change in the signal when no diffusion is included. Full recovery of the magnetization takes place. (D) Changes in the NMR signature of specific groups as a function of the applied gradient field strength are correlated to the diffusion coefficient. (E) Progression of the NMR spectra with changes in the applied field gradient.

unless otherwise specified. To extract the single-particle diffusion coefficient and gain information about the interactions, the scattering data for AuNPs and pure lipoic acid (LA)−poly(ethylene glycol) (PEG) ligands (representative systems) were collected at a few small concentrations.

DOSY-NMR. The technique exploits changes in the net magnetic moment measured by the detector when a sample is subjected to a sequence of pulsed field gradient spin echo (PGSE), schematically depicted in Figure 2. A static magnetic field $\boldsymbol{B}_0$ is first used to align the spins in the sample along the z-axis (in Cartesian coordinates). Then, a 90°× radio frequency (RF) pulse is applied to reorient the spins within the x−y plane, yielding a collective Larmor precession around the z-axis with a frequency

$$\omega_0 = -\gamma \boldsymbol{B}_0 \tag{8}$$

where γ is the gyromagnetic ratio. This produces a set of homogeneously aligned rotating spins with a net nonzero magnetization. Shortly after, a magnetic field gradient pulse with a duration δ is applied to the sample along the z-axis ($\boldsymbol{G}_z$), which disperses the spin precession as a function of their position in the sample (NMR tube), with

$$\omega = -\gamma(B_0 + G_z \cdot r) = \omega_0 + \omega_G \tag{9}$$

This produces a random orientation of the nuclei spins in the x−y plane, which cancel out, yielding a zero total magnetization. After a period τ (from the initial 90°× RF pulse), a second 180°× RF pulse is applied to invert the orientation of the spins, creating a magnetization dispersion that is opposite to the one generated following the first gradient pulse (see Figure 2). Then, a second magnetic field gradient pulse identical to the first one is used to refocus the magnetization, yielding a maximum echo

https://dx.doi.org/10.1021/acs.jpcb.0c02177
J. Phys. Chem. B 2020, 124, 4631−4650

signal collected by the detector. However, in a solution sample, the solute molecules (and their spins) migrate away from their original positions, due to the Brownian motion. This reduces the degree of spin refocusing brought by the second gradient pulse, thereby decreasing the magnetization signal measured by the detector after a period of 2τ (from the first RF pulse). Reduction in the measured signal is thus affected by the combination of gradient strength, its duration δ, the period Δ separating the two gradient pulses, and the magnitude of the diffusion coefficient of the molecules/spins in the sample. In particular, a stronger magnetic field gradient, longer δ, and larger diffusion coefficient reduce refocusing and thus the echo signal measured by the detector.[49−51]

Analysis of the progression of the NMR spectrum of a sample with $\boldsymbol{G}_z$ to extract a measure of the translation diffusion coefficient of solute objects relies on combining the Bloch equation for the magnetization relaxation with the Fick equation for diffusion.[49,50,52−56] We will briefly summarize the mathematical steps leading to the expression relating the measured echo signal vs gradient field strength and diffusion coefficient, but a more detailed description is provided in the Appendix: DOSY-NMR section.

When a sample of spins aligned by a static magnetic field $\boldsymbol{B}_0$ is subjected to a 90°× RF pulse of electromagnetic radiation at the Larmor frequency of the nuclei of interest, its magnetization $\boldsymbol{M}$ is flipped to the x−y plane and experiences a sustained rotation around the z-axis (during relaxation) at the frequency ω_0 (eq 8). If a magnetic field gradient is further applied to the sample along the z-axis, relaxation of the spins will have a position-dependent precession frequency given by eq 9. To treat this relaxation, we divide the vector $\boldsymbol{M}$ into two projections, one along the z-axis, $\boldsymbol{M}_z$, and one in the x−y complex plane, referred to as $\boldsymbol{M}_\perp$ (i.e., $\boldsymbol{M}_\perp = \boldsymbol{M}_x + \mathrm{i}\boldsymbol{M}_y$). Since the detector is placed orthogonal to the direction of $\boldsymbol{B}_0$, only $\boldsymbol{M}_\perp$ contributes to the induction flux and thus to the detected signal. We will focus on the time-dependent relaxation of $\boldsymbol{M}_\perp$, expressed in terms of the Larmor frequency, ω, which accounts for the combined total field $\boldsymbol{B}_0$ and $\boldsymbol{G}_z\cdot\mathbf{r}$, supplemented with the effects of the transverse relaxation T_2

$$M_\perp = M_{\perp 0}\, \mathrm{e}^{\mathrm{i}\omega t - (t/T_2)} \tag{10}$$

with $\boldsymbol{r}$ being the vector position of the spin (in the sample). Here, one can ignore the effects of the transverse relaxation term (or factor them into $\boldsymbol{M}_{\perp 0}$), as done in the original report by Stejskal and Tanner,[49] and further simplify the treatment by transforming the description of the system to a new rotating frame of reference centered at the origin of the Cartesian coordinates.[49,50] These assumptions yield a modified relaxation expression for $\boldsymbol{M}_\perp$, where only the precession involving $\boldsymbol{G}_z$ is kept

$$M_\perp = M_{\perp 0}\, \mathrm{e}^{-\mathrm{i}\gamma G_z\cdot \mathbf{r}t} \tag{11}$$

This can further be used to extract a time-dependent differential equation for the magnetization $\boldsymbol{M}_\perp$

$$\frac{\partial M_\perp}{\partial t} = -\mathrm{i}\gamma G_z\cdot r \times M_{\perp 0}\, \mathrm{e}^{-\mathrm{i}\gamma G_z\cdot rt} = -\mathrm{i}(\gamma G_z\cdot r)M_\perp \tag{12}$$

Taking into account the fact that the field gradient depends on time (i.e., $\boldsymbol{G}_z(t)$ is pulsed) would yield

$$M_\perp = M_{\perp 0}\, \mathrm{e}^{-\mathrm{i}\gamma r\cdot F(t)} \tag{13}$$

where

$$F(t) = \int_0^t G_z(t')\, \mathrm{d}t' \tag{13a}$$

In the absence of diffusion, the above differential equation must be solved throughout the full time window that starts with the application of the 90°× RF pulse ($t = 0$), the first magnetic field gradient of duration δ, the 180°× RF pulse (at $t = \tau$), and the second gradient (also of duration δ) until the signal is collected and analyzed (at $t = 2\tau$), as depicted in Figure 2 (see the Appendix: DOSY-NMR section). In addition, the application of the 180°× RF pulse advances the magnetization vector by twice the angle reached at time $t = \tau$. To account for these factors, a modified expression for the magnetization is considered, where $\boldsymbol{M}_{\perp 0}$ is also time-dependent

$$M_\perp = M_{\perp 0}(t)\, \mathrm{e}^{-\mathrm{i}\gamma r\cdot F(t) - \mathrm{i}\gamma r\cdot(\xi - 1)f} = M_{\perp 0}(t)\, \mathrm{e}^{-\mathrm{i}\gamma r\cdot(F(t) + (\xi - 1)f)} \tag{14}$$

with

$$f = F(\tau),\ \ \xi = 1 \text{ for } t < \tau,\ \text{ and } \xi = -1 \text{ for } t > \tau \tag{14a}$$

Here, the second term in the exponential intervenes only after the application of the 180°× pulse (i.e., a spin echo is formed when $\boldsymbol{F}(2\tau) = 2\boldsymbol{f}$).[49,50]

The effects of diffusion-induced dispersion in the spin precession can be accounted for by expanding eq 12 (above), to include a second term described by the Fick second law involving the spatial variable r (or here z), while maintaining the more general expression for the magnetization solution shown in eq 14, namely, write[49,50]

$$\frac{\partial M_\perp(r, t)}{\partial t} = -\mathrm{i}(\gamma G_z\cdot r)\boldsymbol{M}_\perp + D\nabla^2 M_\perp \tag{15}$$

The first and second terms in the equation can be extracted by applying the time derivative and the Laplacian derivation to the magnetization $\boldsymbol{M}_\perp$, which yields, after a few steps, a final differential equation describing the time dependence involving only the amplitude of the magnetization, $\boldsymbol{M}_{\perp 0}$, due to the Brownian diffusion

$$\frac{\mathrm{d}M_{\perp 0}(t)}{\mathrm{d}t} = -D\gamma^2 M_{\perp 0}(t) \times (F(t) + (\xi - 1)f)^2 \tag{16}$$

This equation has a solution of the form

$$\ln\left(\frac{M_{\perp 0}(2\tau)}{M_{\perp 0}(0)}\right) = -D\gamma^2 \int_0^{2\tau} (F(t) + (\xi - 1)f)^2\, \mathrm{d}t \tag{17}$$

Integration of the terms in the right-hand side of eq 17 must be carried out over the connected discrete domains where the period 2τ is divided into five domains, as shown in Figure 2.[49,50] Furthermore, if we assume that there is no background gradient field, a correct assumption given the advances made over the years in NMR instrumentation and pulse control (see the Appendix: DOSY-NMR section),[50] the integration of the right terms of eq 17 yields

$$\ln\left(\frac{M_{\perp 0}(2\tau)}{M_{\perp 0}(0)}\right) = -\frac{D\gamma^2}{3}(\boldsymbol{G}_z\cdot\delta)^2\{3\Delta - \delta\} \tag{18}$$

which can be rearranged to an expression for the measured intensity as

$$I(2\tau, \boldsymbol{G}_z) = I(0)\, \mathrm{e}^{-D\gamma^2 \boldsymbol{G}_z{}^2\delta^2(\Delta - (\delta/3))} \tag{19}$$

https://dx.doi.org/10.1021/acs.jpcb.0c02177
J. Phys. Chem. B 2020, 124, 4631−4650

Here, we used the relation that the measured intensity, I, is proportional to $M_\perp$. We also note that the pulse sequence requires $\Delta < T_2$ to avoid significant loss in sensitivity.

In our experiment, we use ste to overcome these issues by splitting 180° pulse into two 90° pulse, which allows long Δ delays to be incorporated, limited by T_1 instead of T_2. All DOSY experiments were performed on a Bruker Avance III HD 600 MHz spectrometer equipped with a 5 mm z-gradient broadband observe (BBO) probe at room temperature (293.5 K) using gradient pulse sequences "stebpgp1s" with a 5 s relaxation delay and four dummy scans. The 90° pulse width was calibrated for each DOSY experiment with a typical value over the range of 10−13 s. The gradient duration and diffusion time vary for different sets of samples. The diffusion time depends on the T_2 relaxation times of the proton resonances in the spectrum (∼100−300 ms). Typical experimental parameters used for data obtained from yellow-emitting CdSe−ZnS QDs were as follows: a gradient strength of 45 G/cm, a diffusion time of 200 ms, and a gradient pulse length of 3 ms. Manual baseline corrections were made to minimize the experimental errors.

Other Analytical Measurements. UV−vis absorption spectra were collected using a Shimadzu UV−vis absorption spectrophotometer (UV 2450 model, Shimadzu, Columbia, MD). A fluorolog-3 spectrometer (Jobin Yvon Inc., Edison, NJ) equipped with photomultiplier tube (PMT) and charge-coupled device (CCD) detectors was used to measure the fluorescence spectra. A lab-scale Buchi rotary evaporator R-215 (New Castle, DE) was used to concentrate or dry samples. The photoligation experiments were conducted using a UV photoreactor (model LZC-4 V, Luzchem Research Inc., Ottawa, Canada).

Growth of Colloidal Nanocrystals. *CdSe and CdSe−ZnS Quantum Dots.* The CdSe core-only and CdSe−ZnS core−shell QDs were grown using the "hot injection" method following the steps described in previous literature reports.[5,57−60] Growth of CdSe nanocrystals relied on the reduction of cadmium and selenium precursors at a high temperature (∼350 °C) in a hot coordinating solvent mixture made of tri-*n*-octylphosphineoxide (TOPO), tri-*n*-octylphosphine (TOP), 1-hexadecylamine (HDA), and *n*-hexylphosphonic acid (HPA). Additional details are provided in refs 44, 59, and 60.

The core−shell QDs were prepared by growing ∼6 monolayers of ZnS around the above CdSe core nanocrystals using a mixture of diethylzinc ($ZnEt_2$) and hexamethyldisilathiane ($(TMS)_2S$). Briefly, $ZnEt_2$ and $(TMS)_2S$ precursors were mixed in 3−5 mL of TOP (90%) and then added dropwise to a dispersion of CdSe cores in TOPO (for a final Cd concentration of 0.1−0.5 mM) at a temperature of 150−180 °C, following the protocol described in previous works.[44,59] The size of the core−shell QDs was tuned by varying the core radius while maintaining the same number of ZnS overcoating monolayers. Stock dispersions of core−shell QDs were prepared by adding a mixture of butanol/toluene/hexane to the growth dispersions and then subjecting them to one round of centrifugation at 3500 rpm for ∼15−20 min to remove excess unreacted precursors and other impurities, as previously described.[59]

Oleylamine-Coated Au Nanoparticles. The hydrophobic oleylamine-capped AuNPs (∼10 nm in diameter) used in this study were prepared via hot injection route following the protocol reported by Swihart and co-workers.[61] Briefly, 5 mL of oleylamine was heated under a nitrogen atmosphere to 150 °C in a flask and maintained under refluxing conditions for ∼2−3 h. Separately, a solution made of $HAuCl_4{\cdot}3H_2O$ (0.3 mmol) dissolved in 1 mL of oleylamine was injected into the above flask, and the mixture was further heated for 1.5 h. The reaction mixture progressively developed a pinkish color, indicating the formation of Au nanoparticles. The content was cooled to room temperature, and then one round of centrifugation was applied to remove unreacted precursors and additional insoluble impurities. The dispersion was further diluted with hexane and then stored under room-temperature conditions until further use.

Ligand Exchange and Phase Transfer of the QDs and Au Nanocrystals. The hydrophilic nanocrystals used in this study were prepared via a photoligation strategy that we introduced a few years ago.[62,63] Several ligands made of lipoic acid modified with poly(ethylene glycol) blocks (LA−PEG series or LA−PIMA−PEG) or lipoic acid modified with a zwitterion motif (LA−ZW or LA−PIMA−ZW) were used to coat the nanocolloids and promote their dispersion in aqueous media. Below, we briefly describe a few representative protocols used to photoligate LA−PEG−OCH_3 onto CdSe−ZnS QDs and AuNPs, as well as photoligate LA−ZW onto the same nanocrystals. Additional information can be found in the above references.

Photoligation of QDs and AuNPs with LA−PEG-Based Ligands. *Photoligation of QDs.* First, hydrophobic TOP/TOPO-capped QDs (e.g., 130 μL of ∼21 μM stock dispersion in a hexane/toluene mixture) were precipitated using excess ethanol, followed by centrifugation, yielding a pellet of QD materials. The solvent was removed, and the paste was redispersed in hexane (∼500 μL). Separately, LA−PEG−OCH_3 (100 mg) was dissolved in MeOH (500 μL), and a small quantity of tetramethylammonium hydroxide (TMAH, ∼1 mg) was added. The contents of the two vials were combined in one scintillation vial equipped with a magnetic stir bar, yielding a two-phase solution made of hexane on top (containing the QDs) and methanol at the bottom (containing the ligands). The vial was sealed with a rubber septum, and the atmosphere was switched to nitrogen. This vial was placed inside a UV reactor and irradiated, using a signal with a peak at 350 nm and a power ≅4.5 mW/cm^2, for ∼30−40 min while stirring. A complete phase transfer of the QDs from hexane to methanol occurred. The hexane was removed via a pipette followed by evaporation of MeOH under vacuum. Then, a mixture of chloroform/methanol/hexane (1:1:10 ∼ v/v/v) was added to the QD paste, yielding a precipitate, followed by centrifugation at 3700 rpm for 5 min. The solvent was removed, and the QD paste was gently dried under vacuum and then redispersed in DI water. The aqueous dispersion was passed through a syringe filter (0.45 μm, poly(tetrafluoroethylene) (PTFE)), and further purification of the QDs was carried out by applying a few (two to three) rounds of dilution/concentration using a centrifugal membrane filtration device (MW cutoff = 50 kDa, Amicon Ultra, Millipore) to remove excess solubilized ligands. Following purification, the NPs (QDs) were dispersed in DI water (or methanol if needed) using a clean scintillation vial and stored at 4 °C until further use. The photoligation protocol was applied to coat QDs with other LA-based ligands, such as bis(LA)−PEG−OCH_3 and LA−$(PEG{-}OCH_3)_2$.[62,64]

Photoligation of AuNPs. The protocols were also applied to ligate the PEGylated ligands onto hydrophobic AuNPs.[63] We would, however, like to note that the preparation of hydrophilic AuNPs can also be carried out using conventional approach requiring long incubation time (∼18 h) with the oxidized ligands in the absence of UV irradiation. However, we have

https://dx.doi.org/10.1021/acs.jpcb.0c02177
J. Phys. Chem. B 2020, 124, 4631−4650

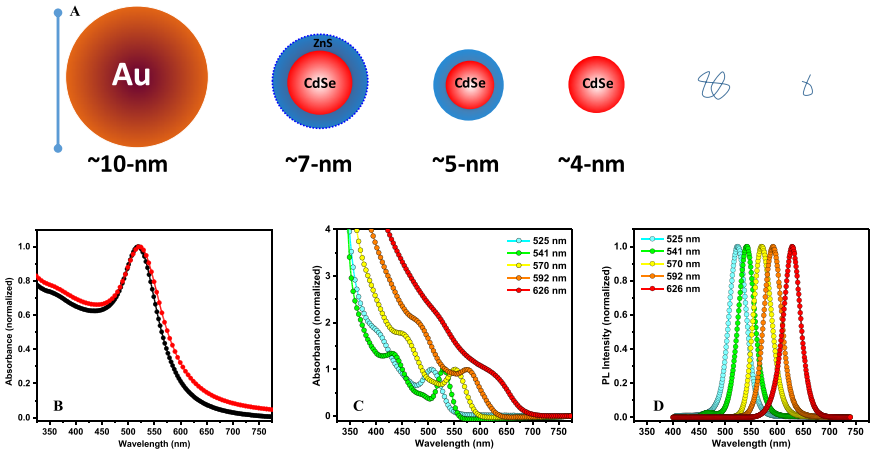

Figure 3. (A) Schematic representation of the various materials investigated: a AuNP, two core−shell QDs, a core-only QD, a polymer, and a short PEG block. (B) UV−vis absorption spectra collected from oleylamine-capped AuNPs dispersed in toluene (black) and LA−PEG−OCH_3-capped AuNPs dispersed in water (red). (C) UV−vis absorption spectra collected from dispersions of CdSe−ZnS QDs in DI water or phosphate buffer. The corresponding photoluminescence (PL) spectra are shown in (D). The absorption spectra are normalized with respect to the SPR value for AuNPs and with respect to the first exciton absorption value for QDs. The PL spectra are normalized with respect to the peak values.

recently found that the photoligation strategy can be effectively applied to cap-exchange oleylamine−AuNPs and other Au nanocolloids with LA-based ligands while requiring much shorter incubation time and less ligands (data not shown).[65] The amounts of ligands used were adjusted based on their molecular weight, to maintain comparable molar excess with respect to the NPs, usually ∼30 000:1 for QDs and ∼300 000:1 for AuNPs.

Photoligation of Oleylamine−AuNPs or QDs with LA−ZW. Preparation of LA−ZW-capped QDs and AuNPs was carried out using essentially the same protocol described above for LA−PEG−OCH_3 ligands, but with a few slight modifications, due to the limited solubility of LA−ZW−QDs and LA−ZW−AuNPs in methanol.[62] We briefly describe the photoligation of oleylamine−AuNPs with LA−ZW. Similar steps were used for coating QDs.[66] In a scintillation vial, 1 mg LA−ZW dissolved in 500 μL MeOH containing ∼1 mg TMAH was added dropwise to a preformed dispersion of AuNPs in hexane (200 μL, 0.09 μM). The molar excess of ligand-to-AuNP was ∼120 000:1. The sample was placed inside the UV reactor and irradiated for 30 min while stirring. Following irradiation, a precipitate of the AuNPs capped with the new zwitterion ligands was formed. The AuNP precipitate was isolated by centrifugation at 3500 rpm for 2−3 min, and then the supernatant was discarded, followed by slight drying under vacuum. The dried AuNP precipitate was dispersed in DI water, passed through a disposable filter (PTFE, 0.45 μm, Millipore), and then excess hydrophilic ligands were removed by applying two to three rounds of dilution/concentration using a centrifugal membrane filtration device (MW cutoff = 50 kDa).[62,66]

Sample Preparation for DLS Experiments. To prepare water-dispersible samples for DLS experiments, the purified aqueous dispersion of nanocrystals was transferred to a cylindrical quartz tube (10 mm optical path) and the concentration was adjusted to ∼1−2 μM for QDs or 50−100 nM for AuNPs, by adding varying amounts of DI water. Samples of hydrophobic nanocrystals (QDs or AuNPs) were prepared by subjecting the growth stock dispersion to two rounds of precipitation using ethanol, a mild drying under vacuum, followed by dispersion in toluene or chloroform. The sample was passed through a disposable filter (0.45 μm, one or two times) to remove dust particles and then used to collect the scattering profiles.

Sample Preparation for NMR Experiments. Preparation of the NMR samples required a slightly more careful purification protocol, to ensure that the used dispersions have a negligible concentration of free ligands; free ligands can contribute to the DOSY-NMR signal but with different diffusion coefficients, complicating data analysis. Typically, to prepare the hydrophilic sample, nanocrystals photoligated with the desired cap were subjected to one round of precipitation allowing isolation of the newly ligated nanocolloid, as described above. The pellet was dried under mild vacuum and then transferred to deuterated water, followed by two to three rounds of concentration/dilution using a centrifugal membrane filtration device (MW cutoff = 50 kDa) with D_2O. In addition to solvent substitution, this also removes excess free solubilized ligands. Finally, the dispersion was loaded onto a 600 MHz NMR tube (5 mm diameter) for data collection. NMR samples of the hydrophobic nanocrystals were prepared by subjecting the growth/stock solution to two rounds of precipitation using ethanol, to remove excess solubilized ligands and precursors. The nanocrystal pellets were thoroughly dried, then dispersed in $CDCl_3$, passed through a syringe filter (0.45 μm), and loaded into 600 MHz NMR tubes as above. Solutions of the ligands (polymer and monomers) were prepared by dissolving the compounds in D_2O for DOSY measurements. The solutions were passed through a 0.45 μm syringe filter before use. Overall, the sample concentration was ∼1−5 μM for QDs and ∼0.2−2 μM for AuNPs.

The concentrations of nanoparticles for both cases were estimated from UV−vis absorption profiles collected from the dispersion, used for DLS or NMR measurements. Specifically, for QDs, the absorbance of the sample at 350 nm was compared to the molar absorption (or extinction) coefficient of the QDs at 350 nm (ε_{350}(QD)) accounting for the UV cell optical path.[42,67] Similarly, the absorbance of the AuNP dispersion at the surface plasmon resonance (SPR) peak was compared to the molar absorption coefficient at 520 nm (ε_{520}(AuNP)).[68]

https://dx.doi.org/10.1021/acs.jpcb.0c02177
J. Phys. Chem. B 2020, 124, 4631−4650

Table 1. Chemical Structure of Organic Ligands Used for the Surface Coating of the Various Nanoparticles. The same $PEG_{750}-OCH_3$ block was used for all compounds, monomers, and polymers

Name	Structure	M_w (g/mol)
TOPO	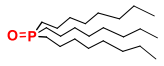	387
TOP	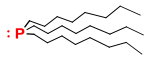	371
HPA	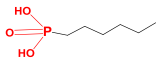	166
HDA	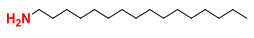	241
LA-PEG-OCH_3	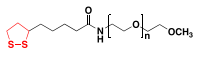	937
Bis(LA)-PEG-OCH_3	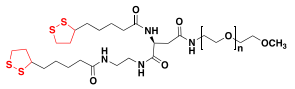	1296
LA-$(PEG-OCH_3)_2$	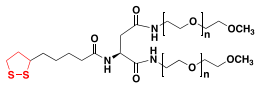	1811
LA_X-PIMA-PEG_Y (X=Y=50%)	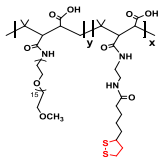	25467
LA-Zwitterion	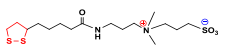	412
LA_X-PIMA-ZW_Y (X=Y=50%)	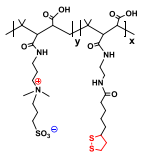	15216

RESULTS AND DISCUSSION

Rationale. The ability of DLS to characterize the diffusion properties of materials with a size range of ∼10−100 nm has made it the method of choice for probing various systems, including polymers, proteins, and inorganic nanocrystals. However, the technique tends to become less effective for very small objects, due to a drastically reduced Rayleigh scattering signal. DOSY, in comparison, exploits changes in the NMR signature of diffusing protons (or other NMR labels) along the magnetic field gradient, G_z, and thus the measurement does not rely on a size-dependent transduction signal.

We hereby provide a side-by-side comparison between data on the diffusion coefficient and the corresponding hydrodynamic radius acquired from the two techniques for three representative materials (see Figure 3): (1) A set of colloidal AuNPs either hydrophobic (grown in the presence of oleylamine cap) or rendered hydrophilic via ligand exchange with a series of lipoic acid-modified ligands (LA appended with a PEG block, LA−PEG−OCH_3; LA appended with a zwitterion group, LA−ZW; LA- and PEG-modified polymers, LA−PIMA−PEG; and LA- and zwitterion-modified polymers, LA−PIMA−ZW). (2) Five sets of core-only and core−shell luminescent QDs stabilized with hydrophobic (alkyl phosphonate and alkylamines) or with PEG-appended lipoic acid ligands. (3) Pure coordinating ligands, namely, LA−PEG−OCH_3 (molecular scale) or LA−PIMA−PEG (a low-molecular-weight polymer). Table 1 provides a summary of the various hydrophobic and hydrophilic coatings used. In particular, we show that both techniques provide comparable data for larger size colloids (AuNPs and core−shell QDs) in hydrophobic and hydrophilic solvents. However, for smaller size objects where the Rayleigh signal becomes very weak, DLS fails to provide meaningful data. DOSY measurements, in comparison, can still provide reliable data on the diffusion coefficient and the hydrodynamic size for larger size colloids, as well as substantially smaller nanocrystals and even molecular-scale ligands. We will also discuss the effects of a few important parameters, such as concentration used, solute object size, and the tracked NMR features, on the comparison between the data extracted from both techniques.

Figure 3 shows the optical absorption spectra collected from dispersions of ∼10 nm AuNPs (in diameter, extracted from TEM) before and after ligand exchange with LA−PEG−OCH_3. The spectra are essentially identical with an SPR peak centered at 519 nm (see Figure 3B). The figure also shows the absorption and emission spectra collected from five sets of LA−PEG−OCH_3-capped CdSe−ZnS QDs with emission at 525 nm

https://dx.doi.org/10.1021/acs.jpcb.0c02177
J. Phys. Chem. B 2020, 124, 4631−4650

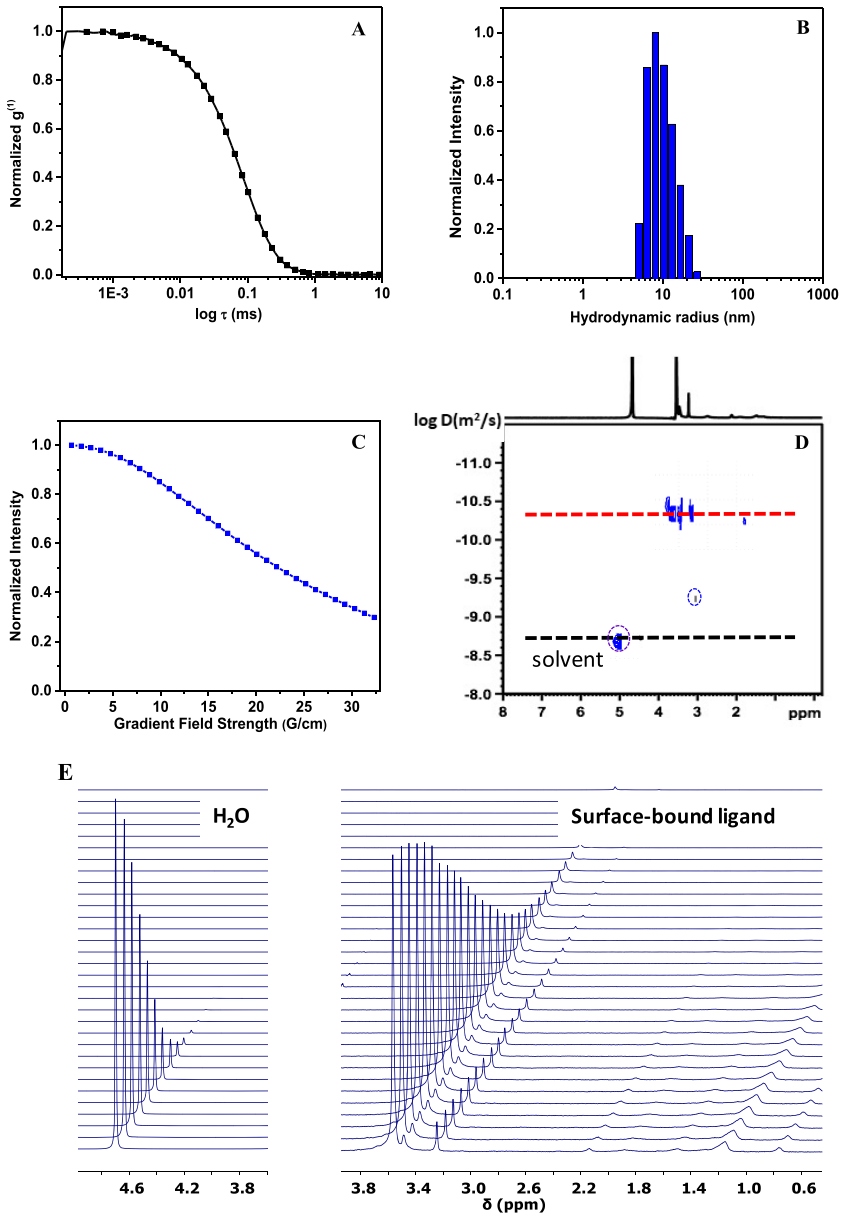

Figure 4. (A, B) Representative plot of the electric field autocorrelation function, $g^{(1)}(\theta,\tau)$ vs $\log(\tau)$, along with a histogram of the intensity vs hydrodynamic radius, R_H; $\theta = 90°$. (C, D) Representative profile of NMR intensity (normalized) vs gradient of the magnetic field strength used, along with the corresponding 2D-NMR DOSY contour plot. The spot outlined in the blue circle at ~3 ppm is attributed to TMAH impurities. The data shown in (C) are extracted from the raw NMR spectra acquired at increasing gradient field strength shown in (E), with a focus on the PEG peak at ~3.6 ppm and terminal methoxy peak at ~3.3 ppm; the spectra showing the water region at 4.7 ppm are also shown. Dispersions of LA−PEG-capped AuNPs in H_2O and in D_2O were used for DLS and DOSY measurement, respectively.

(green), 541 nm (yellow-green), 570 nm (yellow), 592 nm (orange), and 626 nm (red) dispersed in aqueous media; see Figure 3C,D. Similar spectra were collected from the native QDs before phase transfer (data not shown). The excitonic absorption features and narrow emission profiles are preserved for all samples. The absorption and PL spectra collected from hydrophobic CdSe core-only nanocrystals (alkyl-phosphine and alkyl-amine-capped), dispersed in toluene, are shown in the Supporting Information (Figure S1).

Dispersions of Spherical Au Nanocrystals. Figure 4A shows a representative plot of the autocorrelation function $g^{(1)}(\theta,\tau)$ vs $\log(\tau)$, collected from a dispersion of AuNPs ligand-exchanged with LA−PEG−OCH_3 in H_2O ($c \sim 0.01-0.02\ \mu M$), along with the fit using a cumulant series (eq 3). Figure 4B shows the corresponding histogram of intensity vs R_H extracted from the Laplace transform of $g^{(1)}(\theta,\tau)$ (eq 5). A narrow profile with a single peak is measured, indicating that the dispersion is homogeneous, with an average R_H = 10.4 nm and a PDI value of ~0.05−0.1. The data collected from a dispersion of oleylamine−AuNPs in toluene (with similar concentration) are shown in the Supporting Information (Figure S2). Overall, we measure an increase of ~3 nm in R_H following ligand exchange with LA−PEG−OCH_3. This increase results from the combined effects of differences in the ligand size and structure on the contributions of the hydrodynamic interactions to the diffusion properties of oleylamine- or LA−PEG-stabilized AuNPs.[69] Figure 4C shows a plot of the NMR signal vs gradient field strength collected from a dispersion of the same nanocrystals in water, albeit with a

https://dx.doi.org/10.1021/acs.jpcb.0c02177
J. Phys. Chem. B 2020, 124, 4631−4650

concentration of about 1−2 orders of magnitude higher than that used for DLS measurements (c = 0.2−2 μM). The corresponding progression of raw NMR spectra vs $\boldsymbol{G}_z$ is shown in Figure 4E. Figure 4D shows the corresponding DOSY contour spectrum correlating log(D) with the NMR peaks of specific protons in the surface-bound LA−PEG ligands. Clearly, a single diffusion coefficient ($D \cong 4.16 \times 10^{-11}$ m^2/s) is measured, confirming that all of the proton signatures emanate from surface-bound LA−PEG; this value is significantly smaller than the value expected for free LA−PEG (see the sections below).[42] We should note that the ^{1}H NMR spectrum exhibits broadened resonances compared to what is observed for the free ligands.[44] This property is generally attributed to slower transverse spin relaxations resulting from reduced interproton dipolar interactions for surface-coordinated ligands compared to free ones. The R_H value extracted from the D value (combined with eq 6) is ∼9.8 nm. We note that the DOSY spectrum also shows a fast diffusion coefficient ($D \cong 1.87 \times 10^{-9}$ m^2/s), associated with the rapid decay of the NMR signature at 4.7 ppm (shown in Figure 4E) about 2 orders of magnitude faster than the value for ligand-stabilized AuNPs, which we attribute to trace H_2O molecules present in the stock D_2O solvent. This value is close to the one reported in the literature.[70]

Table 2 shows a compiled list of R_H values measured for hydrophobic AuNPs and for the same NPs photoligated with the set of hydrophilic molecules used (including LA−PEG−OCH$_3$, LA−zwitterion, and LA−PIMA−PEG) and dispersed in water, acquired using DLS and DOSY-NMR measurements. Additional details about the sample preparation are described in the Supporting Information. Both DOSY and DLS data indicate that phase transfer consistently increases the overall hydrodynamic size of the nanocrystals compared to oleylamine−AuNPs. Nonetheless, the increase is commensurate with the expected lateral extension of the ligand coordinated on the nanocrystals.[71] Cumulatively, the R_H data collected from both measurements reflect a degree of coating compactness, which depends on the lateral hydrophilic motifs and whether a monomer or a polymer is used, with an overall R_H increase that follows the trend: LA−ZW < LA−PEG ∼ bis(LA)−PEG ∼ LA−(PEG)$_2$ < LA−PIMA−ZW < LA−PIMA−PEG. The compiled data show that there is a good agreement between R_H values acquired from both techniques, indicating that DOSY 2D-NMR provides a reliable measurement for the hydrodynamic size for 10 nm AuNPs under varying conditions and in agreement with DLS data. Additionally, the data in Table 2 show that the DOSY values are consistently slightly smaller than those measured using DLS: R_H(DOSY) are ∼0.5−2 nm smaller than R_H(DLS) values. This observation can be ascribed to differences in the colloid concentrations and will be discussed below.

Table 2. Side-by-Side Comparison of the R_H Values Collected from Dispersions of AuNPs Coated with the Various Listed Ligands, Extracted from DLS and DOSY Measurements[a]

ligand−AuNPs	R_H (nm) from DLS	R_H (nm) from DOSY
oleylamine−AuNPs	7.4	6.9
LA−ZW−AuNPs	8.6	7.3
LA−PEG−AuNPs	10.4	9.8
LA−PIMA−ZW−AuNPs[b]	11.7	11.3
LA−PIMA−PEG−AuNPs	14.9	14.1
LA−(PEG)$_2$−AuNPs	8.7	7.6
bis(LA)−PEG−AuNPs	8.1	7.3

[a]PEG$_{750}$−OCH$_3$ blocks have been used for all measurements. Errors associated with the data extracted from both measurements are 5−8% for DLS data and <10% for DOSY data. [b]This set of AuNPs was not grown under hydrophobic conditions using oleylamine. It used citrate-stabilized NPs grown using the Turkevich method. See the Supporting Information for details about growth and ligand substitution.

Dispersions of CdSe−ZnS Core−Shell Nanocrystals. Figure 5A,B shows a representative plot of $g^{(1)}(\theta,\tau)$ vs log(τ) collected from hydrophobic (TOPO/TOP/HDA/HPA)-capped, CdSe−ZnS QDs dispersed in chloroform (yellow-emitting), along with a histogram of intensity vs R_H acquired from DLS using a nanocrystal concentration of ∼1 μM. Additional profiles collected at different angles are shown in Figure S3, Supporting Information. As noted for AuNPs above, the histogram shows a single peak with PDI ∼ 0.15−0.2. Figure 5C,D shows a typical plot of intensity vs magnetic field gradient strength along with the corresponding DOSY contour spectrum collected from the QD dispersion; a higher concentration (c = 5 μM) was used. Here too, the DOSY-NMR spectrum yields a single diffusion coefficient for the QDs that is about 2 orders of magnitude slower than the one measured for the residual $CHCl_3$ in the $CDCl_3$ solution. Similar data have been collected from the dispersion of hydrophilic core−shell QDs. Figure 5E,F shows a plot of $g^{(1)}(\theta,\tau)$ vs log(τ) collected from LA−PEG-capped core−shell QDs (yellow-emitting) dispersed in water, along with a histogram of the intensity vs R_H; data were acquired using a concentration of ∼1 μM. As shown above, the histogram exhibits a single peak, indicative of homogeneous samples. Figure 5G,H shows a representative profile of the intensity vs magnetic field gradient strength along with the DOSY contour spectrum collected from the same LA−PEG−QDs dispersed in D_2O (at c = 5 μM). The raw NMR vs $\boldsymbol{G}_z$ spectra for these samples (not shown) also exhibit a trend similar to those shown in Figure 4E. Consistent with the data collected for the hydrophobic QDs and AuNPs above, the DOSY contour spectrum shows that a single diffusion coefficient is measured for every proton peak in the one-dimensional (1D) NMR spectrum collected form the QD dispersion. In addition, this diffusion coefficient is much smaller than the one measured for the residual protonated water in the D_2O dispersion. We should stress that the NMR features, which correspond to the slower diffusion coefficient in the DOSY contour plot ascribed to LA−PEG−OCH$_3$−QDs in the medium (namely, peaks at 2.1, 3.2, and 3.5 ppm), are identical to those measured for LA−PEG−OCH$_3$−AuNPs (shown in Figure 4). This consistency provides additional confidence in the DOSY-NMR measurements and their applicability to nanocrystals with various core materials. Additional DOSY contour plots collected from green-emitting core−shell hydrophobic QDs dispersed in $CDCl_3$ or photoligated with LA−PEG or LA−ZW and dispersed in D_2O are provided in Figure S4, Supporting Information.

A compilation of the hydrodynamic radii acquired from DOSY measurements for all sets of core−shell QDs, stabilized with hydrophobic coating, or photoligated with the various hydrophilic ligands, is provided in Table 3. Data show that both techniques consistently yield larger R_H for LA−PEG-capped QDs, which can be attributed to a more pronounced contribution of the hydrophilic ligands to the hydrodynamic interactions compared to the native hydrophobic coating. This is consistent with the data measured for AuNPs and is discussed above.

https://dx.doi.org/10.1021/acs.jpcb.0c02177
J. Phys. Chem. B 2020, 124, 4631−4650

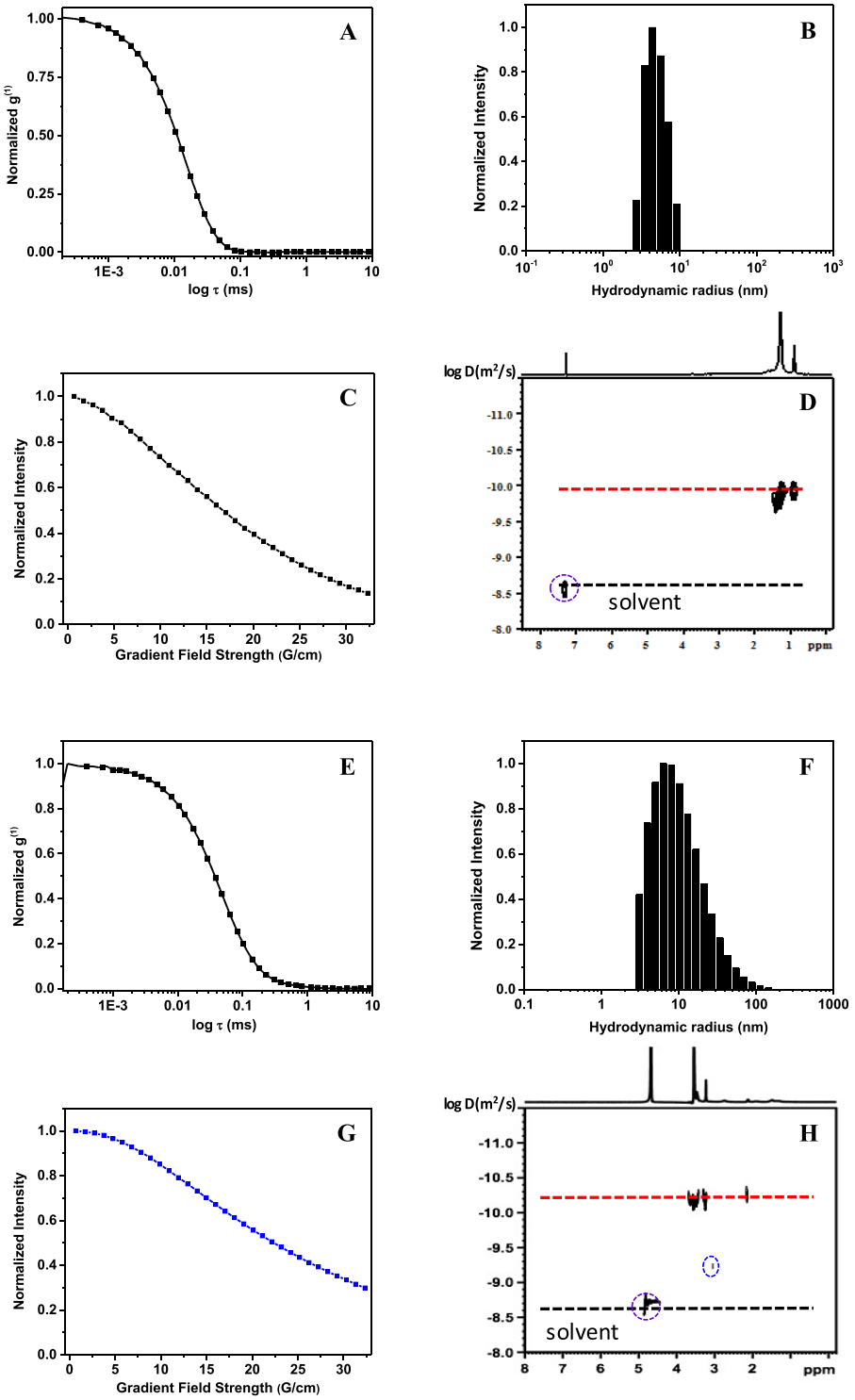

Figure 5. (A) Representative profile of the electric field autocorrelation function $g^{(1)}(\theta,\tau)$ vs $\log(\tau)$ and (B) histogram of the normalized intensity vs hydrodynamic radius collected from yellow-emitting hydrophobic core−shell QDs dispersed in chloroform; data were collected at $\theta = 90°$. (C, D) Representative plots of the normalized intensity vs magnetic field gradient strength, along with the DOSY contour plot collected from the same yellow-emitting QDs dispersed in $CDCl_3$. (E, F) $g^{(1)}(\theta,\tau)$ vs $\log(\tau)$ and histogram of the normalized intensity vs R_H collected from the same QDs after photoligation with LA−PEG and dispersed in water. (G, H) Plots of the intensity vs magnetic field gradient strength, along with the corresponding DOSY contour plot collected from the hydrophilic QDs in D_2O. The spot outlined in the blue circle at ∼3 ppm is attributed to TMAH impurities.

We should note that the ratio between the hydrodynamic radius and inorganic core radius (R_0, extracted from small-angle X-ray scattering, SAXS), R_H/R_0, slightly varies from one sample to another for the series of core−shell QD samples investigated.[27,31] The data shown in Table 3 also indicate that this ratio is consistently larger than 1 and varied between 1.1 and 1.4 for compact ligands (namely, hydrophobic materials). The ratio is larger for QDs capped with LA−PEG ligands, ∼1.6−1.8. A ratio $R_H/R_0 > 1$ is anticipated for such materials, based on predicted contributions of the hydrodynamic interactions to the

https://dx.doi.org/10.1021/acs.jpcb.0c02177
J. Phys. Chem. B 2020, 124, 4631−4650

Table 3. Data on R_H Extracted from DOSY for Core−Shell and Core-Only QDs[a]

λ_{Max} (nm)	R_0 (nm) (core−shell, from SAXS)	R_H (nm): hydrophobic QDs	R_H/R_0	R_H (nm): LA−PEG−QDs	R_H/R_0
525	2.7			4.2	1.6
540	3.1	3.5	1.1	5.7	1.8
570	3.4	3.9	1.1	5.8	1.7
592	3.6	4.5	1.3	6.1	1.7
626	3.9	5.2	1.3	6.8	1.7

[a]Values of R_0, the radius based on SAXS measurements,[27] are also shown. Errors associated with the DOSY data are <10%.

Brownian diffusion as formulated by Oseen for hard spheres.[72] The rather broad range of ratios measured for QDs capped with TOP/TOPO and LA−PEG reflects differences in the contributions of the organic coating. One should note that if fully extended these capping ligands can be as large as, or even larger than, the actual inorganic core material, and their effects cannot be simply viewed as the geometrical sum of the inorganic core and the organic shell.

Dispersions of CdSe Core-Only Nanocrystals. Here, we probe the effects of reducing the nanocrystal size or using fluorescent nanocrystals with emission profile that overlaps with the laser source. For this, dispersions of smaller size core-only QDs (emission peak at 540 nm, $R_0 \sim 1.8$ nm) or red fluorescing nanocrystals (emission band centered at 597 nm, $R_0 \sim 2.3$ nm) were characterized using DLS and DOSY measurements; the emission of the red QDs is broad enough to overlap with the laser signal. The size corresponds to core-only value extracted from SAXS measurements.[27] First, we note that, when DLS is applied to the green-emitting sample, a drastic drop in the generated count rate (~50 kHz) is found, which is below the threshold required for performing reliable DLS experiments. This results from a drop in the Rayleigh scattering signal (which varies as R^6),[29] leading to very low signal-to-noise ratio, which prevents the construction of a useful $g^{(1)}(q,\tau)$ to describe the fluctuation dynamics of the system, as shown in Figure 6A. This has yielded data that could not be well fit to a cumulant series. Conversely, when DLS is applied to red-emitting QD dispersions, it is impossible to construct a reasonable autocorrelation function from the experimental data, despite the rather high signal collected by the APD detector; see Figure 6B. This problem can be attributed to contribution from the QD fluorescence (generated by the He−Ne laser excitation) to the scattered laser signal reaching the detector; this signal has no coherence with the laser signal. Absence of any time coherence between the PL and Rayleigh signals eliminates constructive interference and prevents the buildup of a useful $g^{(1)}(\theta,\tau)$ function. Instead, a rather flat curve is generated, with no memory dependence and an inability to apply cumulant fit to the data (see Figure 6B).

Characterization of these two dispersions using DOSY-NMR, in comparison, yielded more informative data. Indeed, plots of the intensity vs gradient field strength collected from both sets of CdSe QD dispersions (shown in Figure 6C,D) exhibit high signal-to-noise ratios, allowing the buildup of high-quality DOSY contour spectra (see Figure 6E,F). Both spectra show that the diffusion coefficients measured for the QDs are ~1 order of magnitude slower than the value measured for the

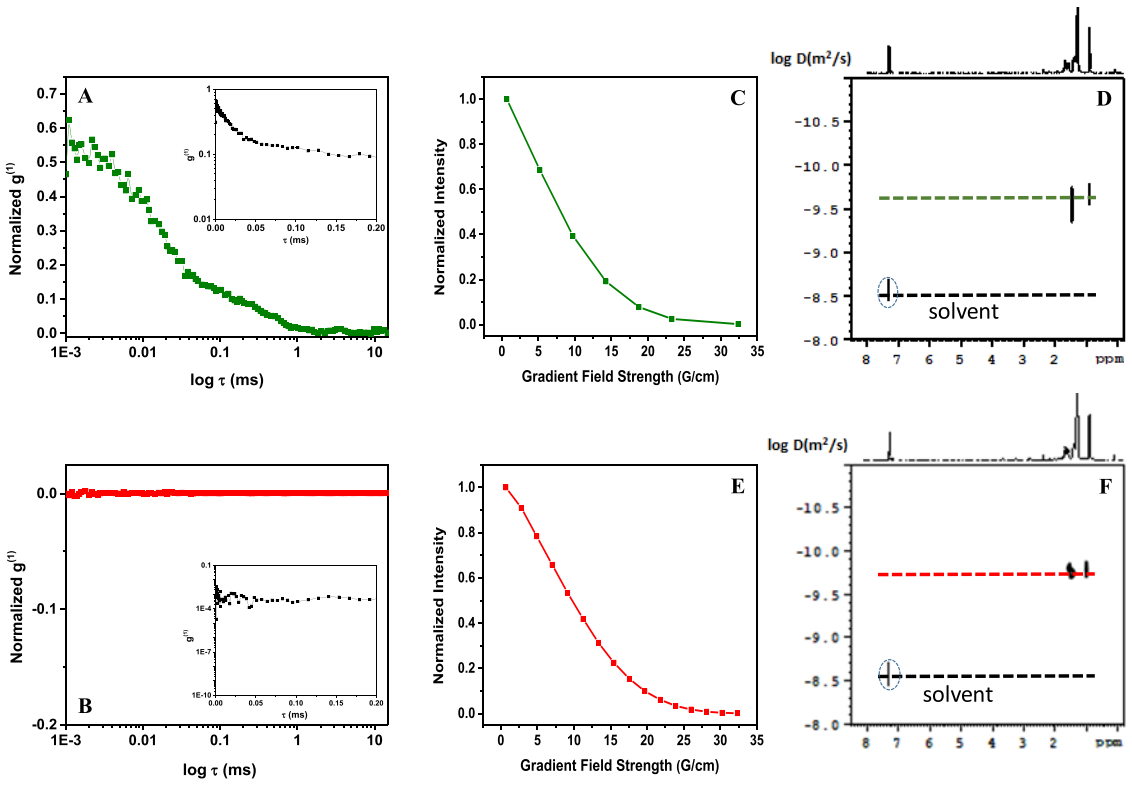

Figure 6. Representative plots of the electric field autocorrelation function $g^{(1)}(\theta,\tau)$ vs $\log(\tau)$ collected from (A) green- and (B) red-emitting CdSe core-only QDs. The insets show $g^{(1)}(\theta,\tau)$ vs τ plots. Representative profiles of the normalized intensity vs magnetic field gradient strength acquired from DOSY measurements, along with the corresponding DOSY contour plots for (C, D) green- and (E, F) red-emitting CdSe QDs dispersed in $CDCl_3$.

https://dx.doi.org/10.1021/acs.jpcb.0c02177
J. Phys. Chem. B 2020, 124, 4631−4650

solvent molecules: D(green QDs) ≅ 1.20×10^{-10} m^2/s, D(red QDs) ≅ 0.97×10^{-10} m^2/s, and $D(CHCl_3) \sim 2.03 \times 10^{-9}$ m^2/s; note that the value for $CHCl_3$ is comparable to that reported in the literature.[39] The corresponding sizes are R_H(green QDs) ≅ 3.4 nm and R_H(red QDs) ≅ 4.2 nm (see Table 4). These results clearly show that DLS has failed to provide useful data on the diffusion coefficient of small size core-only or red fluorescing QDs. In comparison, DOSY-NMR has allowed us to circumvent the constraints encountered by DLS and provided meaningful and practical data. Thus, DOSY provides a highly effective alternative analytical tool for characterizing the Brownian diffusion of very small nanocrystals (radius <2 nm) or fluorescing nanocolloids.

Table 4. Data on the Diffusion Coefficient and Hydrodynamic Size for Core-Only QDs Acquired Using DOSY-NMR[a]

hydrophobic, core-only QDs	R_0 (nm)	$10^{10} \times D$ (m^2/s)	R_H (nm)	R_H/R_0
QDs (λ_{Max} = 540 nm)	1.8	1.20	3.4	1.9
QDs (λ_{Max} = 597 nm)	2.2	0.97	4.2	1.9

[a]$CDCl_3$ was used for these experiments. Values for R_0 are also listed. Errors associated with the DOSY data are <10%.

Molecular-Scale and Oligomer Compounds. Further proof of the effectiveness of DOSY-NMR in probing rather small size solutes is achieved by applying the technique to solutions of LA−PEG−OCH_3 and LA−PIMA−PEG, see the structure in Table 1. The ligands have been dissolved in D_2O at a concentration of ∼50 μM. The panels in Figure 7 show representative plots of the intensity vs strength of the magnetic field gradient together with the corresponding DOSY contour spectra collected from LA−PEG−OCH_3 and LA−PIMA−PEG

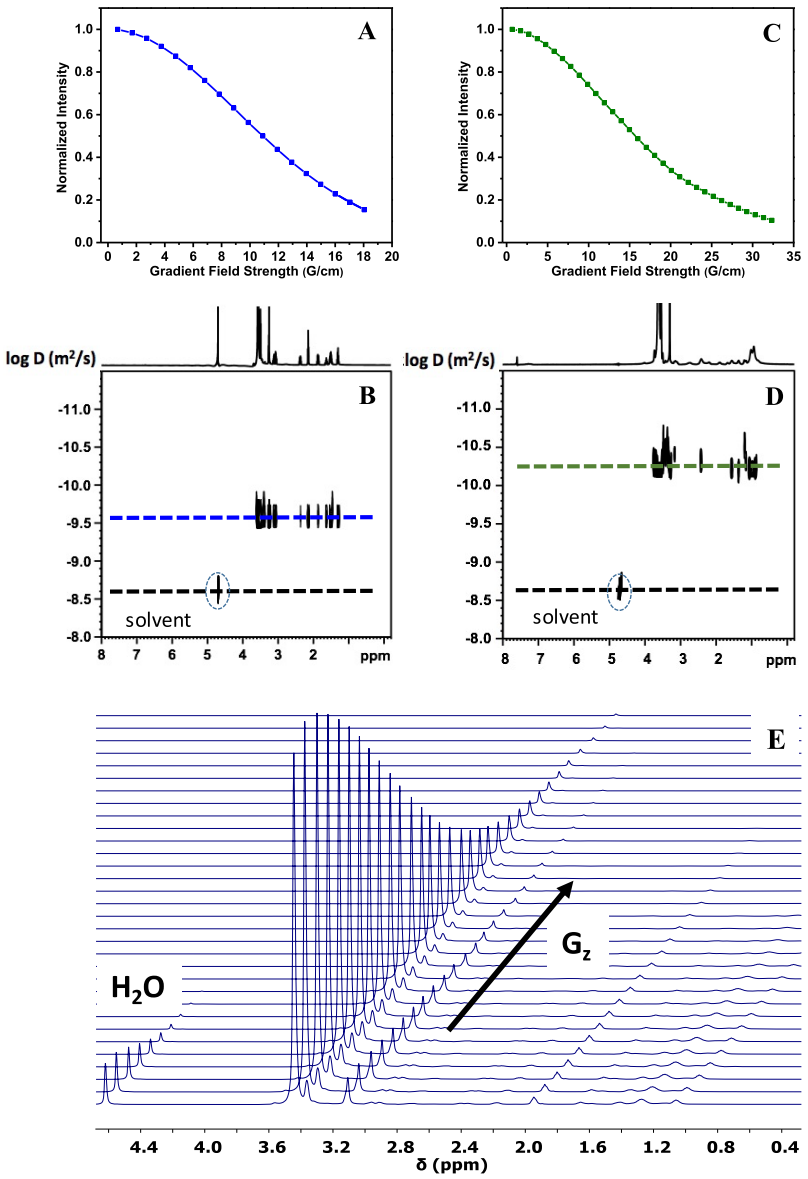

Figure 7. Representative profiles of the intensity (normalized) vs magnetic field gradient strength together with the DOSY contour plots for LA−PEG−OCH_3 (A, B) and LA−PIMA−PEG (C, D) dispersed in D_2O. A representative progression of the raw ^{1}H NMR spectra vs gradient field strength used to extract the profile shown in (A) and (C) is shown in (E). The change in the PEG peak at ∼3.5 ppm was used. The peak at ∼4.7 ppm corresponds to water.

https://dx.doi.org/10.1021/acs.jpcb.0c02177
J. Phys. Chem. B 2020, 124, 4631−4650

solutions. The raw ^{1}H NMR vs G_z spectra collected from LA−PEG−OCH_3 are shown in Figure 7E. Both contour plots show a larger diffusion coefficient ascribed to water molecules, which could also be seen in the NMR spectra shown in Figure 7E. In addition, the DOSY spectra show that there are two slower (but distinct) diffusion coefficients corresponding to the solute ligands: D(LA−PEG−OCH_3) $\cong 1.75 \times 10^{-10}$ m^2/s and D(LA−PIMA−PEG) $\cong 0.62 \times 10^{-10}$ m^2/s; the corresponding R_H values are shown in Table 5. The larger diffusion coefficient measured for LA−PEG reflects the smaller molecular weight of the monomer ligand compared to its polymer counterpart: M_W(LA−PEG) ∼ 937 g/mol and M_W(LA−PIMA−PEG) ∼ 25 467 g/mol.

Table 5. D and R_H Values Extracted for Pure Ligands (LA−PEG−OCH_3 and LA−PIMA−PEG) Dispersed in D_2O Acquired from DOSY-NMR Measurements[a]

sample	$10^{10} \times D$ (m^2/s)	R_H (nm)
LA−PIMA−PEG	0.62	3.6
LA−PEG	1.75	1.3
H_2O	18.9	0.1

[a]Errors associated with the DOSY data are <10%.

We now discuss additional factors that differentiate between the two analytical techniques. DOSY-NMR offers one key advantage when applied to characterize the structure and stoichiometry of ligand coating on nanoscale colloids (such as QDs and AuNPs). Given the ability of the measurement to access a wide range of translational diffusion coefficients, it can be used to distinguish between similar species with different diffusion properties. In particular, it can distinguish between free ligands and those that are nanoparticle-bound in a dispersion. Several groups, including ours, have relied on DOSY-NMR to distinguish the properties of surface-coordinated ligands from those that are freely diffusing in the medium.[25,39,42,44] For instance, we used this strategy to monitor the purification of hydrophobic QDs induced by precipitation/extraction to remove excess free ligands from growth QD dispersions.[44] The above results also indicate that one could distinguish between different molecular species in a mixture of several components, based on the Brownian diffusion, probed by DOSY-NMR spectroscopy. This property is very important and has practical implications in biology and material chemistry.

One should also consider two other differences that can affect the values extracted for the diffusion coefficient. In the first, we use consideration of where the exploited signal in each technique emanates from. DLS relies on the Rayleigh scattering signal from individual objects, which originates from the form factor contribution to the small-angle scattering intensity.[27,30] This term varies as R^6. Thus, DLS tends to overemphasize larger size nanocolloids in a dispersion. Conversely, NMR signal emanates from individual spin nuclei in the ligand molecules. Considering that the density of surface ligands depends on the total area of the nanocrystals, one could assume that the exploited DOSY-NMR intensity varies as $\sim R^2$. This would imply that, in general, the diffusion coefficient for isolated nanocolloids (i.e., infinite dilution) estimated from DLS would be consistently smaller than that measured from DOSY. In the second, we note that the effects of interparticle interactions, though small in sterically stabilized samples, are not negligible. These effects produce a concentration-dependent diffusion coefficient with a linear correction to the value measured for isolated solute objects, in particular, for samples in the dilute regime (see eq 7). Figure 8A shows a plot of D vs concentration, along with a linear fit (eq 7) to the data collected from several LA−PEG−AuNP dispersions ($c \sim 1-10$ nM) extracted from DLS; the increase in D vs c confirms that the dispersions are sterically stabilized. The diffusion coefficient and the hydrodynamic radius of isolated NPs can be extracted from extrapolation at $c = 0$.[29,69] However, in practice, the scattering data are often collected at a single concentration and for a fixed angle ($\theta = 90°$), and then used to extract an estimate for R_H, implying that the apparent data, D_{app} and $R_{H/app}$, are acquired and analyzed. This represents a small error in size data acquired from DLS for sterically stabilized samples, as very small concentrations are often used (dilute regime).[29,31] In contrast,

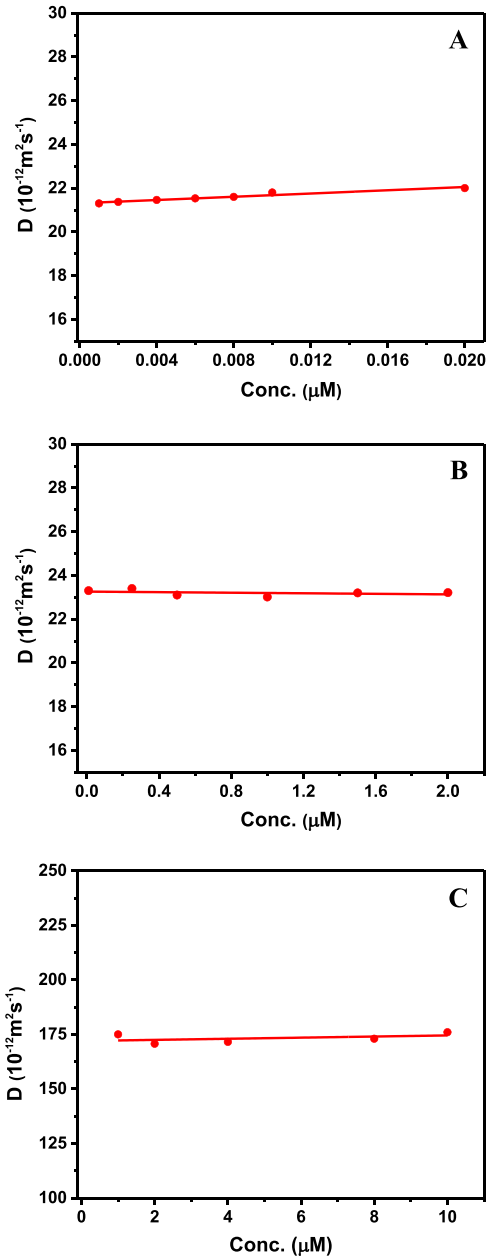

Figure 8. Diffusion coefficient vs concentration, along with a linear fit collected from (A) LA−PEG−AuNP dispersions in water using DLS, (B) LA−PEG−AuNP dispersions in D_2O collected using DOSY, and (C) solutions of LA−PEG in D_2O collected using DOSY.

https://dx.doi.org/10.1021/acs.jpcb.0c02177
J. Phys. Chem. B 2020, 124, 4631−4650

DOSY requires relatively high-concentration samples ($c > 1$ μM) and longer acquisition time to acquire good signal-to-noise ratios, because NMR detectors are much less sensitive than photodetectors used for DLS, such as avalanche photodiode (APD) and even photomultiplier tubes (PMTs). Thus, the apparent values for the diffusion coefficient and hydrodynamic radius (D_{app} and $R_{H/app}$) extracted from DOSY reflect stronger contribution of interparticle interactions, which yield slightly larger values for D (or smaller R_H) compared to those extracted from DLS. The above two considerations are in fact clearly reflected in the values listed in Table 2 and the plots shown in Figure 8A,B; we consistently find that $D_{app/DOSY} > D_{app/DLS}$. This constitutes a small weakness of DOSY compared to DLS, when investigating the Brownian motion of various nanocolloids. This issue is less important for small solute objects such as molecular-scale ligands or small-molecular-weight polymers. Figure 8C shows the diffusion coefficient vs concentration for solutions of LA−PEG−OCH_3 with concentrations of 1−10 μM. Essentially, no change in the measured D was measured.

CONCLUSIONS

We have investigated, side by side, the effectiveness of DLS and DOSY-NMR spectroscopy as analytical techniques to characterize the Brownian diffusion of a wide range of solute materials and under varying conditions. These include dispersions of nanoscale colloids made of AuNPs, luminescent core−shell and core-only QDs, stabilized with various organic coatings, as well as solutions of small-molecular-weight polymers and monomer ligands. Probing such a broad range of samples allowed us to develop a comprehensive comparison between the benefits and limitations of the two analytical techniques that rely on drastically different transduction signals. We find that both techniques are effective for characterizing materials with sizes that are larger than 4 nm and which are not fluorescent. DLS is rapid and requires small concentrations (~nM to μM range), but tends to fail when applied to rather small solute materials (typically objects with radii <2 nm). Conversely, DOSY-NMR is noninvasive and can be applied to a wider range of sizes, including molecular scale and/or fluorescent materials, which demonstrates the great potential of this approach to provide reliable data where other techniques reach their limits. One can also exploit a wide range of nuclei signals (e.g., ^{31}P, ^{19}F, etc.) to apply this technique. DOSY-NMR can discriminate between distinct species in a mixture, based on either difference in the chemical shift (i.e., spectrally), or/and difference in the diffusion coefficient based on size or molecular weight (free vs bound ligands). Less or no effect of impurity on the size extracted from DOSY measurement makes it useful for practical purpose. This can be particularly beneficial for difficult-to-purify samples, such as those used in biology. Nonetheless, because DOSY requires higher solute concentration and well-defined NMR feature(s) to track, it tends to yield values on the diffusion coefficient and hydrodynamic that are more affected by interparticle interactions, compared to DLS.

APPENDIX: DOSY-NMR

DOSY is an NMR spectroscopy technique that exploits changes in the net magnetization of a sample measured by the induction coil detector when the system is subjected to a sequence of pulsed field gradient spin echo (PGSE), as summarized in Figure 2. Typically, a constant magnetic field $\boldsymbol{B}_0$ is first applied to align the spins along the z-axis (in Cartesian coordinates). Then, a 90°× RF pulse is utilized to reorient the spins within the $x-y$ plane, resulting in a precession around the z-axis at the collective Larmor frequency

$$\omega_0 = -\gamma \boldsymbol{B}_0 \tag{A-1}$$

This is followed by the application of a pulse of a magnetic field gradient along the z-axis ($\boldsymbol{G}_z$) to disperse the spin precession as a function of z in the sample, with

$$\omega = -\gamma(\boldsymbol{B}_0 + \boldsymbol{G}_z \cdot r) = \omega_0 + \omega_G \tag{A-2}$$

This dispersion produces a random orientation of the nuclei spins in the $x-y$ plane, which cancel out and yield a zero total magnetization. After a period τ, a second 180°× RF is applied to invert the orientation of the spins in the $x-y$ plane, creating a magnetization dispersion that is opposite to the one generated following the first gradient pulse (see Figure 2). Then, application of a second magnetic field gradient pulse will refocus the spin orientation, yielding a maximum magnetization. However, in a solution sample, the solute molecules and their spins diffuse up and down the sample, due to Brownian motion, which reduces the degree of refocusing achieved and decreases the signal measured by the detector after a period of 2τ from the first RF pulse. The reduction of the signal is affected by the gradient strength, its duration δ, the period Δ, and the diffusion coefficient of the molecules (D). More precisely, a stronger gradient and faster diffusion reduce the magnetization and thus the signal measured at the detector.[49−51] Analysis of the progression of the NMR spectrum of a sample with the magnetic field gradient ($\boldsymbol{G}_z$), to extract a measure of the translation diffusion of solute objects, requires combining the Bloch equation for the magnetization relaxation with the Fick equation for diffusion.[49,50,52−56] Below, we summarize the mathematical rationale and steps required to correlate the measured intensity with the important parameters, namely, $\boldsymbol{G}_z$, δ, Δ, and D.

When a static magnetic field, $\boldsymbol{B}_0$, along the z-axis is applied to a macroscopic sample, the nuclei spins are aligned producing a net magnetization, $\boldsymbol{M}$, along the field. If the sample is further subjected to a 90°× radio-frequency pulse of electromagnetic radiation at the Larmor frequency of the nuclei of interest, the orientation of $\boldsymbol{M}$ is flipped to the $x-y$ plane and experiences a sustained rotation around the z-axis at the frequency (ω_0, eq A-1). If a constant magnetic field gradient is further applied to the sample along the z-axis, the spins will relax with a position-dependent precession frequency given by eq A-2. To treat this relaxation, we divide the magnetization $\boldsymbol{M}$ into two projections, one along the z-axis, $\boldsymbol{M}_z$, and one in the complex $x-y$ plane, referred to as $\boldsymbol{M}_\perp$ (i.e., the $\boldsymbol{M}_\perp = \boldsymbol{M}_x + i\boldsymbol{M}_y$). Since the induction coil detector is placed orthogonal to the direction of $\boldsymbol{B}_0$, only $\boldsymbol{M}_\perp$ contributes to the detected signal. We will focus on the time-dependent relaxation of $\boldsymbol{M}_\perp$, expressed in terms of the Larmor precession frequency, ω, which accounts for the combined total field, $\boldsymbol{B}_0$ and $\boldsymbol{G}_z \cdot \boldsymbol{r}$, supplemented with the effects of the transverse relaxation (with a time constant, T_2)

$$\boldsymbol{M}_\perp = \boldsymbol{M}_{\perp 0}\, e^{i\omega t - (t/T_2)} \tag{A-3}$$

$\boldsymbol{r}$ is the vector position of the spin (in the sample). Analysis can be simplified by ignoring the term accounting for the effects of the transverse relaxation (or by factoring them into $\boldsymbol{M}_{\perp 0}$), as done in the original report by Stejskal and Tanner.[49] An additional simplification of the treatment can be applied by factoring out the effects of the constant precession controlled by $\boldsymbol{B}_0$ (ω_0). This entails transforming the description of the system

https://dx.doi.org/10.1021/acs.jpcb.0c02177
J. Phys. Chem. B 2020, 124, 4631−4650

to a new rotating frame of reference centered at the origin of the Cartesian coordinates.[49,50] This will yield a new relaxation expression for $\boldsymbol{M}_\perp$, where only the precession term involving $\boldsymbol{G}_z$ is kept

$$\boldsymbol{M}_\perp = \boldsymbol{M}_{\perp 0}\, e^{-i\gamma \boldsymbol{G}_z \cdot rt} \tag{A-4}$$

This relation can further be used to extract a time-dependent differential equation for the magnetization $\boldsymbol{M}_\perp$

$$\frac{\partial \boldsymbol{M}_\perp}{\partial t} = -i\gamma \boldsymbol{G}_z \cdot \boldsymbol{r} \times \boldsymbol{M}_{\perp 0}\, e^{-i\gamma \boldsymbol{G}_z \cdot rt} = -i(\gamma \boldsymbol{G}_z \cdot \boldsymbol{r})\boldsymbol{M}_\perp \tag{A-5}$$

which can also be rewritten as

$$\frac{\partial \boldsymbol{M}_\perp}{\boldsymbol{M}_\perp} = -i(\gamma \boldsymbol{G}_z \cdot \boldsymbol{r})\, dt \tag{A-6}$$

Integration of the above equation between 0 and t must take into account the fact that the field gradient depends on time (i.e., $\boldsymbol{G}_z(t)$ is pulsed), yielding an expression for $\boldsymbol{M}_\perp$

$$\boldsymbol{M}_\perp = \boldsymbol{M}_{\perp 0}\, e^{-i\gamma \boldsymbol{r} \cdot \boldsymbol{F}(t)} \tag{A-7}$$

where

$$\boldsymbol{F}(t) = \int_0^t \boldsymbol{G}_z(t')\, dt' \tag{A-8}$$

In the absence of the effects of spin diffusion, the above differential equation must be solved throughout the full time window that starts with the application of the 90°× RF pulse (t = 0), the first magnetic field gradient of duration δ, the 180°× RF pulse (at $t = \tau$), and the second gradient (also of duration δ) until the signal is collected and analyzed (at $t = 2\tau$), as depicted in Figure 2; the two gradients are spaced in time by a period Δ. The transverse magnetization depends on time during the period between t = 0 and 2τ, e.g., immediately following the 90° pulse $\boldsymbol{M}_\perp(t = 0) = \boldsymbol{M}_{\perp 0}$. Additionally, the application of the second 180°× RF pulse advances the magnetization vector by twice the angle reached at time $t = \tau$, thus flipping the magnetization vector in the x−y plane with respect to the z-axis. To account for these factors, a modified expression for the magnetization is used, where $\boldsymbol{M}_{\perp 0}$ is also time-dependent

$$\boldsymbol{M}_\perp = \boldsymbol{M}_{\perp 0}(t)\, e^{-i\gamma \boldsymbol{r} \cdot \boldsymbol{F}(t) - i\gamma \boldsymbol{r} \cdot (\xi - 1)\boldsymbol{f}} = \boldsymbol{M}_{\perp 0}(t)\, e^{-i\gamma \boldsymbol{r} \cdot (\boldsymbol{F}(t) + (\xi - 1)\boldsymbol{f})} \tag{A-9}$$

with

$$\boldsymbol{f} = \boldsymbol{F}(\tau),\ \ \xi = 1 \text{ for } t < \tau,\ \text{ and } \xi = -1 \text{ for } t > \tau \tag{A-10}$$

This expression clearly shows that, while $\boldsymbol{F}(t)$ keeps increasing across the full period between 0 and 2τ, the second term in the exponential intervenes only after the application of the 180°× pulse (i.e., a spin echo is formed when $\boldsymbol{F}(2\tau) = 2\boldsymbol{f}$).[49,50]

The simplest venue for accounting for the effects of diffusion-induced dispersion in the spin precession is to expand the differential equation shown above (eq A-5 or eq 12 in the main text), to include a new term described by the Fick second law involving the spatial variable r, while maintaining the more general expression for the magnetization solution shown in eq A-5, namely, write[49,50]

$$\frac{\partial \boldsymbol{M}_\perp(\boldsymbol{r}, t)}{\partial t} = -i(\gamma \boldsymbol{G}_z \cdot \boldsymbol{r})\boldsymbol{M}_\perp + D\nabla^2 \boldsymbol{M}_\perp \tag{A-11}$$

The left term in the equation can be extracted by applying the time derivative to $\boldsymbol{M}_\perp$, which yields

$$\frac{\partial \boldsymbol{M}_\perp(\boldsymbol{r}, t)}{\partial t} = \frac{d\boldsymbol{M}_{\perp 0}(t)}{dt}\, e^{-i\gamma \boldsymbol{r} \cdot (\boldsymbol{F}(t) + (\xi - 1)\boldsymbol{f})} - \boldsymbol{M}_{\perp 0}(t) i\gamma \boldsymbol{r}. \left(\frac{d\boldsymbol{F}(t)}{dt} + (\xi - 1)\frac{d\boldsymbol{f}}{dt}\right) e^{-i\gamma \boldsymbol{r} \cdot (\boldsymbol{F}(t) + (\xi - 1)\boldsymbol{f})} \tag{A-12}$$

Using the identities, $\frac{d\boldsymbol{f}}{dt} = 0$ and $\frac{d\boldsymbol{F}(t)}{dt} = \boldsymbol{G}(t)$, the above expression becomes

$$\frac{\partial \boldsymbol{M}_\perp(\boldsymbol{r}, t)}{\partial t} = \frac{d\boldsymbol{M}_{\perp 0}(t)}{dt}\, e^{-i\gamma \boldsymbol{r} \cdot (\boldsymbol{F}(t) + (\xi - 1)\boldsymbol{f})} - \boldsymbol{M}_{\perp 0}(t) i\gamma \boldsymbol{r} \cdot \boldsymbol{G}(t)\, e^{-i\gamma \boldsymbol{r} \cdot (\boldsymbol{F}(t) + (\xi - 1)\boldsymbol{f})} \tag{A-13}$$

Similarly, applying the Laplacian derivation to the magnetization, with respect to the variable $\boldsymbol{r}$, yields

$$D\nabla^2 \boldsymbol{M}_\perp = D\boldsymbol{M}_{\perp 0}(t)\nabla^2 [e^{-i\gamma \boldsymbol{r} \cdot (\boldsymbol{F}(t) + (\xi - 1)\boldsymbol{f})}]$$

$$D\nabla^2 \boldsymbol{M}_\perp = D\boldsymbol{M}_{\perp 0}(t)(-i\gamma(\boldsymbol{F}(t) + (\xi - 1)\boldsymbol{f})) \times \nabla [e^{-i\gamma \boldsymbol{r} \cdot (\boldsymbol{F}(t) + (\xi - 1)\boldsymbol{f})}]$$

$$D\nabla^2 \boldsymbol{M}_\perp = -D\gamma^2 \boldsymbol{M}_{\perp 0}(t)(\boldsymbol{F}(t) + (\xi - 1)\boldsymbol{f})^2 e^{-i\gamma \boldsymbol{r} \cdot (\boldsymbol{F}(t) + (\xi - 1)\boldsymbol{f})} \tag{A-14}$$

Plugging the relations eqs A-13 and A-14 into eq A-11 would yield

$$\frac{\partial \boldsymbol{M}_\perp(\boldsymbol{r}, t)}{\partial t} = \frac{d\boldsymbol{M}_{\perp 0}(t)}{dt}\, e^{-i\gamma \boldsymbol{r} \cdot (\boldsymbol{F}(t) + (\xi - 1)\boldsymbol{f})} - \boldsymbol{M}_{\perp 0}(t)(i\gamma \boldsymbol{r} \cdot G(t))\, e^{-i\gamma \boldsymbol{r} \cdot (\boldsymbol{F}(t) + (\xi - 1)\boldsymbol{f})} = -\boldsymbol{M}_{\perp 0}(t)(i\gamma \boldsymbol{r} \cdot \boldsymbol{G}_z)\, e^{-i\gamma \boldsymbol{r} \cdot (\boldsymbol{F}(t) + (\xi - 1)\boldsymbol{f})} - D\gamma^2 \boldsymbol{M}_{\perp 0}(t)(\boldsymbol{F}(t) + (\xi - 1)\boldsymbol{f})^2 e^{-i\gamma \boldsymbol{r} \cdot (\boldsymbol{F}(t) + (\xi - 1)\boldsymbol{f})} \tag{A-15}$$

which can be simplified to yield the final differential equation describing the time-dependent changes in the amplitude of the magnetization, $\boldsymbol{M}_{\perp 0}$, due to the Brownian diffusion

$$\frac{d\boldsymbol{M}_{\perp 0}(t)}{dt} = -D\gamma^2 \boldsymbol{M}_{\perp 0}(t) \times (\boldsymbol{F}(t) + (\xi - 1)\boldsymbol{f})^2 \tag{A-16}$$

and

$$\frac{d\boldsymbol{M}_{\perp 0}(t)}{\boldsymbol{M}_{\perp 0}(t)} = -D\gamma^2 (\boldsymbol{F}(t) + (\xi - 1)\boldsymbol{f})^2\, dt \tag{A-17}$$

If integrated between t = 0 and 2τ

$$\int_0^{2\tau} \frac{d\boldsymbol{M}_{\perp 0}(t)}{\boldsymbol{M}_{\perp 0}(t)} = -D\gamma^2 \int_0^{2\tau} (\boldsymbol{F}(t) + (\xi - 1)\boldsymbol{f})^2\, dt \tag{A-18}$$

it yields

$$\ln\left(\frac{\boldsymbol{M}_{\perp 0}(2\tau)}{\boldsymbol{M}_{\perp 0}(0)}\right) = -D\gamma^2 \int_0^{2\tau} (\boldsymbol{F}(t) + (\xi - 1)\boldsymbol{f})^2\, dt \tag{A-19}$$

Using the pulse pattern shown in Figure 2 and the conditions summarized in eq A-10, one can divide the integration into two terms, one over the range $\{0, \tau)$ and the other over $(\tau, 2\tau)$, and simplify the above expression as

https://dx.doi.org/10.1021/acs.jpcb.0c02177
J. Phys. Chem. B 2020, 124, 4631−4650

$$\ln\left(\frac{\boldsymbol{M}_{\perp 0}(2\tau)}{\boldsymbol{M}_{\perp 0}(0)}\right) = -D\gamma^2 \int_0^{2\tau} (\boldsymbol{F}(t) + (\xi - 1)\boldsymbol{f})^2 \, dt \tag{A-20}$$

$$\ln\left(\frac{\boldsymbol{M}_{\perp 0}(2\tau)}{\boldsymbol{M}_{\perp 0}(0)}\right) = -D\gamma^2\left\{\int_0^{\tau} \boldsymbol{F}(t)^2 \, dt + \int_{\tau}^{2\tau} (\boldsymbol{F}(t) - 2\boldsymbol{f})^2 \, dt\right\} \tag{A-21}$$

$$\ln\left(\frac{\boldsymbol{M}_{\perp 0}(2\tau)}{\boldsymbol{M}_{\perp 0}(0)}\right) = -D\gamma^2\left\{\int_0^{\tau} \boldsymbol{F}(t)^2 \, dt + \int_{\tau}^{2\tau} (\boldsymbol{F}(t)^2 - 4\boldsymbol{f}\boldsymbol{F}(t) + 4f^2) \, dt\right\} \tag{A-22}$$

$$\ln\left(\frac{\boldsymbol{M}_{\perp 0}(2\tau)}{\boldsymbol{M}_{\perp 0}(0)}\right) = -D\gamma^2\left\{\int_0^{\tau} \boldsymbol{F}(t)^2 \, dt + \int_{\tau}^{2\tau} \boldsymbol{F}(t)^2 \, dt - 4\boldsymbol{f}\cdot\int_{\tau}^{2\tau} \boldsymbol{F}(t) \, dt + 4\boldsymbol{f}^2\tau\right\} \tag{A-23}$$

$$\ln\left(\frac{\boldsymbol{M}_{\perp 0}(2\tau)}{\boldsymbol{M}_{\perp 0}(0)}\right) = -D\gamma^2\left\{\int_0^{2\tau} \boldsymbol{F}(t)^2 \, dt - 4\boldsymbol{f}.\int_{\tau}^{2\tau} \boldsymbol{F}(t) \, dt + 4\boldsymbol{f}^2\tau\right\} \tag{A-24}$$

The key here is to carry out the integration of the terms on the right-hand side of eq A-24 over connected discrete domains, as shown in Figure 2. For this, we separate the period 2τ into five domains, as done in the original reports.[49,50] We further assume that there is no background gradient field. This assumption is correct given the advances made over the years in NMR instrumentation and pulse control, yielding[50]

$$\boldsymbol{F}_1(t) = 0 \text{ for } 0 \le t < t_1 \tag{A-25a}$$

because there is no background field gradient

$$\boldsymbol{F}_2(t) = \boldsymbol{F}_1(t_1) + \int_{t_1}^{t} \boldsymbol{G}_z(t') \, dt' \text{ for } t_1 \le t < t_1 + \delta \tag{A-25b}$$

$$\boldsymbol{F}_3(t) = \boldsymbol{F}_2(t_1 + \delta) \text{ for } t_1 + \delta \le t < t_1 + \Delta \tag{A-25c}$$

$$\boldsymbol{F}_4(t) = \boldsymbol{F}_3(t_1 + \Delta) + \int_{t_1+\Delta}^{t} \boldsymbol{G}_z(t') \, dt' \text{ for } t_1 + \Delta \le t < t_1 + \delta + \Delta \tag{A-25d}$$

$$\boldsymbol{F}_5(t) = \boldsymbol{F}_4(t_1 + \Delta + \delta) \text{ for } t_1 + \Delta + \delta \le t \tag{A-25e}$$

We then use these five integrals to determine the three terms on the right-hand side of eq A-24

- Term 1, $\left[\int_0^{2\tau} \boldsymbol{F}^2(t) \, dt\right]$, becomes

$$\int_0^{2\tau} \boldsymbol{F}^2(t) \, dt = \int_0^{t_1} \boldsymbol{F}_1^2(t) \, dt + \int_{t_1}^{t_1+\delta} \boldsymbol{F}_2^2(t) \, dt + \int_{t_1+\delta}^{t_1+\Delta} \boldsymbol{F}_3^2(t) \, dt + \int_{t_1+\Delta}^{t_1+\Delta+\delta} \boldsymbol{F}_4^2(t) \, dt + \int_{t_1+\Delta+\delta}^{2\tau} \boldsymbol{F}_5^2(t) \, dt = \frac{1}{3}(-(\boldsymbol{G}_z\cdot\delta)^2(12t_1 + 7\delta + 9\Delta - 24\tau)) \tag{A-26}$$

- Term 2,

$$-4\boldsymbol{f}\cdot\int_{\tau}^{2\tau} \boldsymbol{F}(t) \, dt = -4F_3(\tau)\cdot\left(\int_{\tau}^{t_1+\Delta} \boldsymbol{F}_3(t) \, dt + \int_{t_1+\Delta}^{t_1+\Delta+\delta} \boldsymbol{F}_4(t) \, dt + \int_{t_1+\Delta+\delta}^{2\tau} \boldsymbol{F}_5(t) \, dt\right)$$

becomes

$$= 2(\boldsymbol{G}_z\delta)^2 \times (2t_1 + \delta + 2\Delta - 6\tau) \tag{A-27}$$

- Term 3

$$4\boldsymbol{f}^2\tau = 4\boldsymbol{F}_3^2(\tau)\tau = 4\tau(\boldsymbol{G}_z\cdot\delta)^2 \tag{A-28}$$

Adding these terms between {} on the right-hand side of eq A-24 yields

$$\ln\left(\frac{\boldsymbol{M}_{\perp 0}(2\tau)}{\boldsymbol{M}_{\perp 0}(0)}\right) = -\frac{1}{3}(\boldsymbol{G}_z\cdot\delta)^2\{12t_1 + 7\delta + 9\Delta - 24\tau - 12t_1 - 6\delta - 12\Delta + 36\tau - 12\tau\} = -\frac{1}{3}(\boldsymbol{G}_z\cdot\delta)^2\{\delta - 3\Delta\} \tag{A-29}$$

Then, eq A-24 becomes

$$\ln\left(\frac{\boldsymbol{M}_{\perp 0}(2\tau)}{\boldsymbol{M}_{\perp 0}(0)}\right) = -D\gamma^2\left[-\frac{1}{3}(\boldsymbol{G}_z\cdot\delta)^2\{\delta - 3\Delta\}\right] \tag{A-29a}$$

This expression can be rewritten as

$$\ln\left(\frac{\boldsymbol{M}_{\perp 0}(2\tau)}{\boldsymbol{M}_{\perp 0}(0)}\right) = -D\gamma^2\boldsymbol{G}_z^2\delta^2\left(\Delta - \frac{\delta}{3}\right) \tag{A-30}$$

or

$$\boldsymbol{M}_{\perp 0}(2\tau) = \boldsymbol{M}_{\perp 0}(0)\, e^{-D\gamma^2\boldsymbol{G}_z^2\delta^2(\Delta-(\delta/3))} \tag{A-31}$$

This relation can be expressed as

$$I(2\tau, \boldsymbol{G}_z) = I(0)\, e^{-D\gamma^2\boldsymbol{G}_z^2\delta^2(\Delta-(\delta/3))} \tag{A-32}$$

where $I(2\tau,\boldsymbol{G}_z)$ designates the echo intensity measured by the detector at the end of the PGSE pulse sequence. We should note that a separation between the two gradient pulses $\Delta < T_2$ is required to avoid significant loss in the sensitivity of the measurement.

■ ASSOCIATED CONTENT

Supporting Information

The Supporting Information is available free of charge at https://pubs.acs.org/doi/10.1021/acs.jpcb.0c02177.

https://dx.doi.org/10.1021/acs.jpcb.0c02177
J. Phys. Chem. B 2020, 124, 4631−4650

Material information, additional experimental details, QD and AuNP growth, synthesis of the monomer and polymer ligands, additional UV−vis absorption and PL spectra, and additional DLS profiles and DOSY contour plots (PDF)

AUTHOR INFORMATION

Corresponding Author

Hedi Mattoussi − *Department of Chemistry and Biochemistry, Florida State University, Tallahassee, Florida 32306, United States;* orcid.org/0000-0002-6511-9323; Email: mattoussi@chem.fsu.edu

Authors

Chengqi Zhang − *Department of Chemistry and Biochemistry, Florida State University, Tallahassee, Florida 32306, United States*

Zhicheng Jin − *Department of Chemistry and Biochemistry, Florida State University, Tallahassee, Florida 32306, United States*

Birong Zeng − *Department of Chemistry and Biochemistry, Florida State University, Tallahassee, Florida 32306, United States;* orcid.org/0000-0003-1582-4929

Wentao Wang − *Department of Chemistry and Biochemistry, Florida State University, Tallahassee, Florida 32306, United States;* orcid.org/0000-0003-2273-4171

Goutam Palui − *Department of Chemistry and Biochemistry, Florida State University, Tallahassee, Florida 32306, United States*

Complete contact information is available at: https://pubs.acs.org/10.1021/acs.jpcb.0c02177

Notes

The authors declare no competing financial interest.

ACKNOWLEDGMENTS

The authors thank Florida State University, the National Science Foundation (NSF-CHE, Grant 1508501), AFOSR (Grant #FA9550-18-1-0144), and Asahi-Kasei for financial support. The authors also thank Sisi Wang and Liang Du for the fruitful discussions.

REFERENCES

(1) Gaponenko, S. V. *Optical Properties of Semiconductor Nanocrystals*; Cambridge University Press: Cambridge, 1998; p 245.

(2) Medintz, I.; Uyeda, H.; Goldman, E.; Mattoussi, H. Quantum dot bioconjugates for imaging, labelling and sensing. *Nat. Mater.* **2005**, *4*, 435−446.

(3) Michalet, X.; Pinaud, F. F.; Bentolila, L. A.; Tsay, J. M.; Doose, S.; Li, J. J.; Sundaresan, G.; Wu, A. M.; Gambhir, S. S.; Weiss, S. Quantum dots for live cells, in vivo imaging, and diagnostics. *Science* **2005**, *307*, 538−544.

(4) Klimov, V. I. *Nanocrystal Quantum Dots*, 2nd ed.; CRC Press: Boca Raton, 2010; p 469.

(5) Talapin, D. V.; Lee, J. S.; Kovalenko, M. V.; Shevchenko, E. V. Prospects of Colloidal Nanocrystals for Electronic and Optoelectronic Applications. *Chem. Rev.* **2010**, *110*, 389−458.

(6) Kovalenko, M. V.; Manna, L.; Cabot, A.; Hens, Z.; Talapin, D. V.; Kagan, C. R.; Klimov, V. I.; Rogach, A. L.; Reiss, P.; Milliron.; et al. Prospects of Nanoscience with Nanocrystals. *ACS Nano* **2015**, *9*, 1012−1057.

(7) Boles, M. A.; Ling, D.; Hyeon, T.; Talapin, D. V. The surface science of nanocrystals. *Nat. Mater.* **2016**, *15*, 141−153.

(8) Kagan, C. R.; Lifshitz, E.; Sargent, E. H.; Talapin, D. V. Building devices from colloidal quantum dots. *Science* **2016**, *353*, No. aac5523.

(9) Hildebrandt, N.; Spillmann, C. M.; Algar, W. R.; Pons, T.; Stewart, M. H.; Oh, E.; Susumu, K.; Díaz, S. A.; Delehanty, J. B.; Medintz, I. L. Energy Transfer with Semiconductor Quantum Dot Bioconjugates: A Versatile Platform for Biosensing, Energy Harvesting, and Other Developing Applications. *Chem. Rev.* **2017**, *117*, 536−711.

(10) Liu, Z.; Yuan, J.; Hawks, S. A.; Shi, G.; Lee, S.-T.; Ma, W. Photovoltaic Devices Based on Colloidal PbX Quantum Dots: Progress and Prospects. *Solar RRL* **2017**, *1*, No. 1600021.

(11) Resch-Genger, U.; Grabolle, M.; Cavaliere-Jaricot, S.; Nitschke, R.; Nann, T. Quantum dots versus organic dyes as fluorescent labels. *Nat. Methods* **2008**, *5*, 763−775.

(12) Mattoussi, H.; Palui, G.; Na, H. B. Luminescent quantum dots as platforms for probing in vitro and in vivo biological processes. *Adv. Drug Delivery Rev.* **2012**, *64*, 138−166.

(13) Wegner, K. D.; Jin, Z.; Lindén, S.; Jennings, T. L.; Hildebrandt, N. Quantum-Dot-Based Förster Resonance Energy Transfer Immunoassay for Sensitive Clinical Diagnostics of Low-Volume Serum Samples. *ACS Nano* **2013**, *7*, 7411−7419.

(14) Howes, P. D.; Chandrawati, R.; Stevens, M. M. Colloidal nanoparticles as advanced biological sensors. *Science* **2014**, *346*, No. 1247390.

(15) Rahme, K.; Chen, L.; Hobbs, R. G.; Morris, M. A.; O'Driscoll, C.; Holmes, J. D. PEGylated gold nanoparticles: polymer quantification as a function of PEG lengths and nanoparticle dimensions. *RSC Adv.* **2013**, *3*, 6085−6094.

(16) Silvi, S.; Credi, A. Luminescent sensors based on quantum dot-molecule conjugates. *Chem. Soc. Rev.* **2015**, *44*, 4275−4289.

(17) Bruns, O. T.; Bischof, T. S.; Harris, D. K.; Franke, D.; Shi, Y.; Riedemann, L.; Bartelt, A.; Jaworski, F. B.; Carr, J. A.; et al. Next-generation in vivo optical imaging with short-wave infrared quantum dots. *Nat. Biomed. Eng.* **2017**, *1*, No. 0056.

(18) Goldman, E. R.; Clapp, A. R.; Anderson, G. P.; Uyeda, H. T.; Mauro, J. M.; Medintz, I. L.; Mattoussi, H. Multiplexed toxin analysis using four colors of quantum dot fluororeagents. *Anal. Chem.* **2004**, *76*, 684−688.

(19) Wu, X. Y.; Liu, H. J.; Liu, J. Q.; Haley, K. N.; Treadway, J. A.; Larson, J. P.; Ge, N. F.; Peale, F.; Bruchez, M. P. Immunofluorescent labeling of cancer marker Her2 and other cellular targets with semiconductor quantum dots. *Nat. Biotechnol.* **2003**, *21*, 41−46.

(20) Lee, J.; Sharei, A.; Sim, W. Y.; Adamo, A.; Langer, R.; Jensen, K. F.; Bawendi, M. G. Nonendocytic Delivery of Functional Engineered Nanoparticles into the Cytoplasm of Live Cells Using a Novel, High-Throughput Microfluidic Device. *Nano Lett.* **2012**, *12*, 6322−6327.

(21) Röcker, C.; Pötzl, M.; Zhang, F.; Parak, W. J.; Nienhaus, G. U. A quantitative fluorescence study of protein monolayer formation on colloidal nanoparticles. *Nat. Nanotechnol.* **2009**, *4*, 577−580.

(22) Treuel, L.; Brandholt, S.; Maffre, P.; Wiegele, S.; Shang, L.; Nienhaus, G. U. Impact of Protein Modification on the Protein Corona on Nanoparticles and Nanoparticle−Cell Interactions. *ACS Nano* **2014**, *8*, 503−513.

(23) Hoshino, A.; Fujioka, K.; Oku, T.; Suga, M.; Sasaki, Y. F.; Ohta, T.; Yasuhara, M.; Suzuki, K.; Yamamoto, K. Physicochemical properties and cellular toxicity of nanocrystal quantum dots depend on their surface modification. *Nano Lett.* **2004**, *4*, 2163−2169.

(24) Jeong, S.; Achermann, M.; Nanda, J.; Ivanov, S.; Klimov, V. I.; Hollingsworth, J. A. Effect of the Thiol−Thiolate Equilibrium on the Photophysical Properties of Aqueous CdSe/ZnS Nanocrystal Quantum Dots. *J. Am. Chem. Soc.* **2005**, *127*, 10126−10127.

(25) Green, M. The nature of quantum dot capping ligands. *J. Mater. Chem.* **2010**, *20*, 5797−5809.

(26) Brown, P. R.; Kim, D.; Lunt, R. R.; Zhao, N.; Bawendi, M. G.; Grossman, J. C.; Bulović, V. Energy Level Modification in Lead Sulfide Quantum Dot Thin Films through Ligand Exchange. *ACS Nano* **2014**, *8*, 5863−5872.

(27) Mattoussi, H.; Cumming, A. W.; Murray, C. B.; Bawendi, M. G.; Ober, R. Properties of CdSe nanocrystal dispersions in the dilute

regime: Structure and interparticle interactions. *Phys. Rev. B* **1998**, *58*, 7850−7863.
(28) Murray, C. B.; Kagan, C. R.; Bawendi, M. G. Synthesis and characterization of monodisperse nanocrystals and close-packed nanocrystal assemblies. *Annu. Rev. Mater. Sci.* **2000**, *30*, 545−610.
(29) Berne, B. J.; Pecora, R. *Dynamic Light Scattering: With Applications to Chemistry, Biology, and Physics*; Dover Publications: Mineola, NY, 2000; 376 p.
(30) Brown, W. *Dynamic Light Scattering: The Method and Some Applications*; Clarendon Press: Oxford, 1993.
(31) Pons, T.; Uyeda, H. T.; Medintz, I. L.; Mattoussi, H. Hydrodynamic dimensions, electrophoretic mobility, and stability of hydrophilic quantum dots. *J. Phys. Chem. B* **2006**, *110*, 20308−20316.
(32) Hill, D.; Ast, C.; Lohmannsroben, H. G.; Zulqurnain, A.; Parak, W.; Hildebrandt, N. In *Size Determination of Quantum Dots with Fluorescence Correlation Spectroscopy*, Colloidal Quantum Dots/Nanocrystals for Biomedical Applications VI, 2011; Vol. *7909*.
(33) Pristinski, D.; Kozlovskaya, V.; Sukhishvili, S. A. Fluorescence correlation spectroscopy studies of diffusion of a weak polyelectrolyte in aqueous solutions. *J. Chem. Phys.* **2005**, *122*, No. 014907.
(34) Petrášek, Z.; Hoege, C.; Mashaghi, A.; Ohrt, T.; Hyman, A. A.; Schwille, P. Characterization of Protein Dynamics in Asymmetric Cell Division by Scanning Fluorescence Correlation Spectroscopy. *Biophys. J.* **2008**, *95*, 5476−5486.
(35) Dominguez-Medina, S.; Chen, S.; Blankenburg, J.; Swanglap, P.; Landes, C. F.; Link, S. Measuring the Hydrodynamic Size of Nanoparticles Using Fluctuation Correlation Spectroscopy. *Annu. Rev. Phys. Chem.* **2016**, *67*, 489−514.
(36) Moreels, I.; Fritzinger, B.; Martins, J. C.; Hens, Z. Surface Chemistry of Colloidal PbSe Nanocrystals. *J. Am. Chem. Soc.* **2008**, *130*, 15081−15086.
(37) Fritzinger, B.; Capek, R. K.; Lambert, K.; Martins, J. C.; Hens, Z. Utilizing Self-Exchange To Address the Binding of Carboxylic Acid Ligands to CdSe Quantum Dots. *J. Am. Chem. Soc.* **2010**, *132*, 10195−10201.
(38) Drijvers, E.; De Roo, J.; Martins, J. C.; Infante, I.; Hens, Z. Ligand Displacement Exposes Binding Site Heterogeneity on CdSe Nanocrystal Surfaces. *Chem. Mater.* **2018**, *30*, 1178−1186.
(39) Hens, Z.; Martins, J. C. A Solution NMR Toolbox for Characterizing the Surface Chemistry of Colloidal Nanocrystals. *Chem. Mater.* **2013**, *25*, 1211−1221.
(40) Hens, Z.; Moreels, I.; Martins, J. C. In Situ 1H NMR Study on the Trioctylphosphine Oxide Capping of Colloidal InP Nanocrystals. *ChemPhysChem* **2005**, *6*, 2578−2584.
(41) Van Lokeren, L.; Maheut, G.; Ribot, F.; Escax, V.; Verbruggen, I.; Sanchez, C.; Martins, J. C.; Biesemans, M.; Willem, R. Characterization of Titanium Dioxide Nanoparticles Dispersed in Organic Ligand Solutions by Using a Diffusion-Ordered Spectroscopy-Based Strategy. *Chem. − Eur. J.* **2007**, *13*, 6957−6966.
(42) Zhang, C.; Palui, G.; Zeng, B.; Zhan, N.; Chen, B.; Mattoussi, H. Non-Invasive Characterization of the Organic Coating of Biocompatible Quantum Dots Using Nuclear Magnetic Resonance Spectroscopy. *Chem. Mater.* **2018**, *30*, 3454−3466.
(43) Wang, W.; Ji, X.; Kapur, A.; Zhang, C.; Mattoussi, H. A Multifunctional Polymer Combining the Imidazole and Zwitterion Motifs as a Biocompatible Compact Coating for Quantum Dots. *J. Am. Chem. Soc.* **2015**, *137*, 14158−14172.
(44) Zeng, B.; Palui, G.; Zhang, C.; Zhan, N.; Wang, W.; Ji, X.; Chen, B.; Mattoussi, H. Characterization of the Ligand Capping of Hydrophobic CdSe−ZnS Quantum Dots Using NMR Spectroscopy. *Chem. Mater.* **2018**, *30*, 225−238.
(45) Rayleigh, L. On the transmission of light through an atmosphere containing small particles in suspension, and on the origin of the blue of the sky. *London, Edinburgh, Dublin Philos. Mag. J. Sci.* **1899**, *47*, 375−384.
(46) Bhattacharjee, S. DLS and zeta potential − What they are and what they are not? *J. Controlled Release* **2016**, *235*, 337−351.
(47) Mattoussi, H.; Karasz, F. E.; Langley, K. H. Electrostatic and screening effects on the dynamic aspects of polyelectrolyte solutions. *J. Chem. Phys.* **1990**, *93*, 3593−3603.
(48) Koppel, D. E. Analysis of Macromolecular Polydispersity in Intensity Correlation Spectroscopy: The Method of Cumulants. *J. Chem. Phys.* **1972**, *57*, 4814−4820.
(49) Stejskal, E. O.; Tanner, J. E. Spin Diffusion Measurements: Spin Echoes in the Presence of a Time-Dependent Field Gradient. *J. Chem. Phys.* **1965**, *42*, 288−292.
(50) Kuchel, P. W.; Pagès, G.; Nagashima, K.; Velan, S.; Vijayaragavan, V.; Nagarajan, V.; Chuang, K. H. Stejskal−tanner equation derived in full. *Concepts Magn. Reson., Part A* **2012**, *40A*, 205−214.
(51) Tanner, J. E. Use of the Stimulated Echo in NMR Diffusion Studies. *J. Chem. Phys.* **1970**, *52*, 2523−2526.
(52) Cohen, Y.; Avram, L.; Frish, L. Diffusion NMR Spectroscopy in Supramolecular and Combinatorial Chemistry: An Old Parameter—New Insights. *Angew. Chem., Int. Ed.* **2005**, *44*, 520−554.
(53) Sinnaeve, D. The Stejskal−Tanner equation generalized for any gradient shape—an overview of most pulse sequences measuring free diffusion. *Concepts Magn. Reson., Part A* **2012**, *40A*, 39−65.
(54) Avram, L.; Cohen, Y. Diffusion NMR of molecular cages and capsules. *Chem. Soc. Rev.* **2015**, *44*, 586−602.
(55) Groves, P. Diffusion ordered spectroscopy (DOSY) as applied to polymers. *Polym. Chem.* **2017**, *8*, 6700−6708.
(56) Li, W.; Chung, H.; Daeffler, C.; Johnson, J. A.; Grubbs, R. H. Application of 1H DOSY for Facile Measurement of Polymer Molecular Weights. *Macromolecules* **2012**, *45*, 9595−9603.
(57) Murray, C. B.; Norris, D. J.; Bawendi, M. G. Synthesis and characterization of nearly monodisperse CdE (E = S, Se, Te) semiconductor nanocrystallites. *J. Am. Chem. Soc.* **1993**, *115*, 8706−8715.
(58) Dabbousi, B. O.; Rodriguez-Viejo, J.; Mikulec, F. V.; Heine, J. R.; Mattoussi, H.; Ober, R.; Jensen, K. F.; Bawendi, M. G. (CdSe)ZnS core-shell quantum dots: Synthesis and characterization of a size series of highly luminescent nanocrystallites. *J. Phys. Chem. B* **1997**, *101*, 9463−9475.
(59) Clapp, A. R.; Goldman, E. R.; Mattoussi, H. Capping of CdSe-ZnS quantum dots with DHLA and subsequent conjugation with proteins. *Nat. Protoc.* **2006**, *1*, 1258−1266.
(60) Qu, L. H.; Peng, Z. A.; Peng, X. G. Alternative routes toward high quality CdSe nanocrystals. *Nano Lett.* **2001**, *1*, 333−337.
(61) Liu, S.; Chen, G.; Prasad, P. N.; Swihart, M. T. Synthesis of Monodisperse Au, Ag, and Au−Ag Alloy Nanoparticles with Tunable Size and Surface Plasmon Resonance Frequency. *Chem. Mater.* **2011**, *23*, 4098−4101.
(62) Palui, G.; Avellini, T.; Zhan, N.; Pan, F.; Gray, D.; Alabugin, I.; Mattoussi, H. Photoinduced Phase Transfer of Luminescent Quantum Dots to Polar and Aqueous Media. *J. Am. Chem. Soc.* **2012**, *134*, 16370−16378.
(63) Jin, Z.; Kapur, A.; Wang, W.; Hernandez, J. D.; Thakur, M.; Mattoussi, H. The dual−function of lipoic acid groups as surface anchors and sulfhydryl reactive sites on polymer−stabilized QDs and Au nanocolloids. *J. Chem. Phys.* **2019**, *151*, No. 164703.
(64) Aldeek, F.; Hawkins, D.; Palomo, V.; Safi, M.; Palui, G.; Dawson, P. E.; Alabugin, I.; Mattoussi, H. UV and Sunlight Driven Photoligation of Quantum Dots: Understanding the Photochemical Transformation of the Ligands. *J. Am. Chem. Soc.* **2015**, *137*, 2704−2714.
(65) ten Hove, J. B.; Schijven, L. M. I.; Wang, J.; Velders, A. H. Size-controlled and water-soluble gold nanoparticles using UV-induced ligand exchange and phase transfer. *Chem. Commun.* **2018**, *54*, 13355−13358.
(66) Zhan, N.; Palui, G.; Mattoussi, H. Preparation of compact biocompatible quantum dots using multicoordinating molecular-scale ligands based on a zwitterionic hydrophilic motif and lipoic acid anchors. *Nat. Protoc.* **2015**, *10*, 859−874.
(67) Leatherdale, C. A.; Woo, W. K.; Mikulec, F. V.; Bawendi, M. G. On the absorption cross section of CdSe nanocrystal quantum dots. *J. Phys. Chem. B* **2002**, *106*, 7619−7622.

https://dx.doi.org/10.1021/acs.jpcb.0c02177
J. Phys. Chem. B 2020, 124, 4631−4650

(68) Liu, X.; Atwater, M.; Wang, J.; Huo, Q. Extinction coefficient of gold nanoparticles with different sizes and different capping ligands. *Colloids Surf., B* **2007**, *58*, 3−7.
(69) Wang, W.; Ji, X.; Du, L.; Mattoussi, H. Enhanced Colloidal Stability of Various Gold Nanostructures Using a Multicoordinating Polymer Coating. *J. Phys. Chem. C* **2017**, *121*, 22901−22913.
(70) Holz, M.; Heil, S. R.; Sacco, A. Temperature-dependent self-diffusion coefficients of water and six selected molecular liquids for calibration in accurate ^{1}H NMR PFG measurements. *Phys. Chem. Chem. Phys.* **2000**, *2*, 4740−4742.
(71) Ji, X.; Wang, W.; Mattoussi, H. Effects of separation distance on the charge transfer interactions in quantum dot-dopamine assemblies. *Phys. Chem. Chem. Phys.* **2015**, *17*, 10108−10117.
(72) Landau, L. D.; Lifshits, E. M. *Fluid Mechanics*; Elsevier Butterworth-Heinemann: Amsterdam, 2012; Vol. *6*.

https://dx.doi.org/10.1021/acs.jpcb.0c02177
J. Phys. Chem. B 2020, 124, 4631−4650